NOVEL INSIGHTS INTO OLFACTORY BULB GAMMA OSCILLATIONS

A Dissertation

Presented to the Faculty of the Graduate School

of Cornell University

In Partial Fulfillment of the Requirements for the Degree of

Doctor of Philosophy

by

Shane Thomas Peace

August 2015

NOVEL INSIGHTS INTO OLFACTORY BULB GAMMA OSCILLATIONS

Shane Thomas Peace, Ph. D.

Cornell University 2015

In the rodent olfactory bulb (OB), coherent gamma oscillations (40-100 Hz) in the local field potential are readily observed during active odor investigation and are thought to be necessary for high resolution odorant constructions. These oscillations are believed to be coordinated by dendrodendritic connections in the external plexiform layer (EPL) where the excitatory mitral cells receive inhibitory, GABAergic feedback from granule cells. Currently, the predominant theories of gamma oscillation rhythmogenesis are insufficient to fully describe the complex characteristics of bulbar gamma oscillations. The goal of the presented research was to utilize novel recording techniques to more fully describe the network mechanisms that generate gamma oscillations in the rodent OB. To investigate synchronous activity in the OB, we recorded from OB slices from mice coexpressing channelrhodopsin-2 and enhanced yellow fluorescent protein under the control of the olfactory marker protein, hence limiting expression to the olfactory sensory neuron axonal arbors innervating the glomerular layer of the slices. To enable large area recordings across the olfactory bulb slice, we used a 60-electrode planar microelectrode array to record spike and local field activity. A brief (5 second) flash (4 Hz) of a blue light stimulus or the brief application of metabotropic glutamate receptor agonists and an acetylcholine receptor agonist were used to induce long-lasting (>5 minutes) gamma oscillations (20-55Hz) that were coherent across ranges of up to 300 μm across the OB slice. Contrary to current theories of OB gamma oscillogenesis, blocking bulbar GABA(A) receptor activity did not reduce the power of the gamma band oscillations but did reduce the

oscillation frequency. Furthermore, GABAergic blockade eliminated the coherence between oscillating glomerular columns. To explain these results, I propose a hybrid coupled-oscillator model of bulbar oscillogenesis, in which lateral GABAergic feedback couples and synchronizes independent intraglomerular oscillators that rely on non-GABAergic coordination mechanisms, primarily mitral cell subthreshold oscillations (STOs). These STOs function to synchronize the spiking of the mitral cells. Our model predicts the gamma oscillation frequency is influenced by the repetitive GABAergic reset of mitral cell STOs increasing the overall frequency of the oscillatory network. Extensive GABAergic feedback across the external plexiform layer is further necessary to synchronize the intraglomerular oscillations across the bulb producing the coherent gamma oscillations recorded *in vivo*. To increase the resolution of electrophysiological recordings within the bulbar region producing coherent oscillations, we developed a 768-channel MEA designed with decreased distance between recording electrodes. Our MEA also employed angle sensitive pixels that are optical receptors capable of detecting and reconstructing the patterns of optical stimulation used to excite the transgenic slices. These sensors were positioned among the recording electrodes of the MEA in order to combine optical and electrophysiological recordings.

BIOGRAPHICAL SKETCH

Shane Thomas Peace was born in Shreveport, Louisiana on November 3rd, 1980. There he developed a deep sense of privacy.

For my family: past and future.

ACKNOWLEDGMENTS

This dissertation is the product of seven years of collaboration, discussion, and support from many mentors, colleagues, and friends. I am indebted and deeply thankful to all of those that helped bring together these research projects and provided personal support throughout graduate school. First, I would like to thank my advisor, Thomas Cleland. Thom has provided many years of relentless excitement towards scientific discovery that was critical during the more confusing “GABA Shane” days of establishing the groundwork for this dissertation. He has a seemingly endless supply of patience, especially when providing feedback for my writing, and an ability to connect and communicate a myriad of details in exciting ways that was a constant reminder of why research is fun. I am also greatly appreciative of the other members of my special committee. Christiane Linster, co-PI of the CPL, has the remarkable ability to pinpoint critical details and asked many tough, thought provoking questions that has made working in the CPL a truly enjoyable and stimulating atmosphere. Joe Fetcho has been very generous with his lab space, advice, and the much appreciated honest critiques. Al Molnar has been an exciting committee member and co-PI on the collaborative MEA project that pushed me to conduct risky experiments that I was hesitant to conduct. Although not a committee member, I want to thank Ben Johnson, Al’s graduate student, in this upper category of acknowledgements who I worked closely with on the MEA project until his graduation. Not only did Ben become a good friend, but he was an absolutely critical contributor through his MATLAB support and regular doses of doubt at the incremental steps of the research progress that became this dissertation. Although mostly random, I couldn’t have picked a better collaborator.

A large part of the learning atmosphere and support in graduate school is directly attributable to the graduate student and postdoc interactions. Amina

Kinkhabwala and Sandeep Kishore spent a considerable amount of time helping me to prepare for the sink or swim style Cellular and Molecular Journal Club. My best friend Dan helped me to think more critically about the sense of smell. Martin von Arx, John Olthoff, Jason Gallant, and Boris Chagnaud helped to redefine the complexity of "just one beer." Matt "Department Store" Lewis and Joseph DiPietro have done an excellent job of finely interweaving critical feedback with wide-open, unfiltered rants during conversations about research snags or graduate school obstacles. Kevin Loope has been a dear friend that always provided thoughtful conversation and helped to sing backup during the necessary belting of Janis Joplin. Although not part of the student or postdoc community, Dawn and Geoff Potter have treated me like family and I will always be grateful for their generosity, chicken, and GABA(A) facilitation.

My parents, Nicki and Freddie Peace, were always encouraging of my decisions and provided an atmosphere of unconditional support. Families grow and inevitably change. Now, Nicki and Gary Arthur have maintained this unconditional support, even through the communication blackouts, and for this I must express great gratitude.

Lastly, it is difficult to summarize all of the ways my life has been improved by the addition of Olga Escanilla. Thom Cleland put it best when he said, "Everything is better with an Olga." I have yet to find a better description of this wonderful woman.

TABLE OF CONTENTS

PREFACE

A fundamental question in neuroscience is how the brain coordinates its massive amount of activity across spatially segregated regions. One window into the brain's organizational features is to look for evidence of synchronized activity. The questions addressed by the following body of research are centered on the rhythmic gamma oscillations that are widely recorded across the brain of many species of animals. Gamma oscillations are a periodic rhythm in a recorded electrophysiological signal typically found between 30-80 Hz. These oscillations are studied in multiple electrophysiological signals. Raw signals recorded from neural tissue can be high-passed filtered to extract the high frequency components of electrophysiological signals such as action potentials (APs). Cross correlations between AP times recorded from neurons across the brain can be analyzed for evidence of gamma band synchronization, whereas autocorrelations of AP trains are studied for indications of periodicity within cellular firing patterns.

On the other hand, local field potentials (LFPs) can be extracted from raw recordings of excitable neural tissue by low-pass filtering the raw data and extracting the slowly oscillating, weakly electric field potentials. All of the recorded data discussed in the following chapters are from the analysis of LFPs. These extracellularly recorded signals are important because rhythmic LFP activity is indicative of underlying synchronization among the multitude of synaptic currents that alone would be too small to record. It takes a network of synchronized activity to produce this weakly electric field potential that would quickly dissipate across the extracellular space if not coordinated by periodic processes.

While gamma band oscillations in the LFP are conspicuously indicative of underlying synchronization, it is important to address the role of this synchronization. A useful, categorical way to discuss AP and LFP relationships is that APs are the

output of an excited network and the resulting LFP is the coordinated input to a region of the brain. It is widely regarded that the biophysical processes necessary to produce synchronized activity underlying the recorded gamma band oscillations are the hallmarks of network constraint on the AP timing and synchronization. This population level constraint on the temporal patterning of output is considered to be fundamentally important for the receiving areas of AP propagation. The conversion of rate based metrics, commonly associated with the transduction of sensory stimuli, can be converted to a temporal metric considered to be more metabolically efficient and further utilizing the spike timing regimes of synaptic plasticity.

The importance of studying gamma oscillations in the brain arises from the necessity to improve our understanding of how information is packaged and moved throughout the brain. For example, recordings from the olfactory bulb (OB) of rats forced to discriminate between two similar odorants produced an increase in gamma band power compared to easier discrimination tasks between two very different odorants. This example illustrates the point that the underlying network activity producing gamma band oscillations is associated with increasing the level of information available downstream. In the preceding example, this increase in gamma activity leads to an increased resolution of odorant constructions. The question arises, if this rhythmic synchronization is important, how does the olfactory bulb produce rhythmic, synchronous activity?

Gamma oscillations recorded in the olfactory bulb are typically recorded in the 40 – 100 Hz range and are coherent, meaning the oscillations are phase-locked across the olfactory bulbs. According to current source density analysis of olfactory bulb gamma oscillations, the primary source of power for the oscillations comes from the external plexiform layer (EPL) where the dendrodendritic synapses between mitral cells and granule cells are found. Mitral cells are the large excitatory output cells of

the olfactory bulb and granule cells are a large population of inhibitory cells that provide GABAergic feedback following excitation by the mitral cells.

The circuit mechanisms that underlie olfactory bulb gamma oscillations have traditionally been hypothesized to consist of a combination of excitatory- inhibitory (E-I) interactions similar to the pyramidal – interneuron network gamma (PING) connections considered to coordinate gamma oscillations in the cortex. Support for this E-I model is due to the known synaptic connectivity where these oscillations are recorded, the external plexiform layer (EPL), that is comprised of interactions between the excitatory mitral cells and the inhibitory granule cells. One predictive weakness of the E-I model, however, is that the frequency in these models is determined by the excitatory drive to the excitatory cells in the E-I network. The makes the E-I model insufficient to explain the coherent gamma oscillations recorded in the OB in the presence of heterogeneous levels of input as the result of complex odor environments. Odors produce a myriad of activity across the OB which would be difficult to cohere if a pure E-I network was responsible for OB gamma oscillations.

Furthermore, the membrane voltage of the MCs undergo subthreshold oscillations (STOs) that dictate a preferred range of firing frequencies and that govern the timing of MC spikes. Classic PING models work best with simple Hodgkin-Huxley described cells and are generally modeled using simple integrate-and-fire neurons. This means that E-I type networks are less robust when presented with various cellular "personalities."

Secondly, another dominant theory of gamma oscillation mechanism is called the interneuron-network gamma (ING) or the inhibitory-inhibitory (I-I) network. These circuitry mechanisms are strongly supported to underlie hippocampal gamma oscillations. The biophysical properties of I-I oscillations are better capable of producing synchronization across more heterogeneous levels of input, but the granule

cell layer of the olfactory bulb does not show evidence of I-I circuitry. The inhibitory granule cells do not communicate with each other in a way necessary for a functional I-I network and the other inhibitory cells of the granule cell layer do not present the necessary synaptic connections to support this model.

Due to the insufficiency of the current models to fully predict the complex dynamics of bulbar gamma oscillations recorded *in vivo*, further research is required to better explain the intricate interactions of olfactory bulb circuitry. Therefore, the goal of the research presented in this dissertation is to establish the network mechanisms that underlie gamma oscillations in the rodent olfactory bulb

CHAPTER 1

HYBRID COUPLED-OSCILLATOR MECHANISM GENERATES COHERENT GAMMA OSCILLATIONS IN THE OLFACTORY BULB

Shane T. Peace[1*], Benjamin C. Johnson[2], Guoshi Li[3], Martin Kaiser[4], Izumi Fukunaga[4-5], Andreas T. Schaefer[4-5], Alyosha C. Molnar[2], Thomas A. Cleland[3*]

[1]Dept. Neurobiology & Behavior

[2]Dept. Electrical and Computer Engineering

[3]Dept. Psychology

Cornell University

Ithaca, NY 14853

[4]Behavioural Neurophysiology

Max Planck Institute for Medical Research

Heidelberg, Germany

[5]Division of Neurophysiology

MRC National Institute for Medical Research

London, UK

Introduction

Local field potential oscillations in the "gamma" frequency band (~30-80 Hz) have been studied for decades across many regions of the brain, including the olfactory bulb (OB). Physiologically, gamma oscillations evince synchronized periodic activity across some population of neurons within the recorded field; this synchronous activity can constrain action potential timing in principal neurons and reduce noise correlations across neuronal populations [1–5], and thereby regulate spike timing-dependent computations and plasticity [4,6,7]. These data underlie current hypotheses that the OB, in addition to biasing the content and increasing the selectivity of odor representations [8,9], also transforms the *metric* of sensory information from a rate-coded basis among primary olfactory sensory neurons (OSNs) into a sparser, spike timing-based representation at the output of the OB [5,7], thereby gaining all the attendant advantages of this coding scheme[10]. Implicit in these theories of timing-based computation in the OB, critically, is the principle that gamma oscillations are substantially coherent across the entire olfactory bulb [11–13]. However, synchronizing neuronal populations robustly enough to construct timing-based representations is nontrivial. For example, the frequency of network oscillations under some mechanisms of oscillogenesis depends on principal neuron activation levels (e.g., [14,15]), such that the heterogeneous activation patterns that encode odor identity may paradoxically impair the temporal coordination necessary to construct timing-based representations of this afferent information. Consequently, to test these foundational coding hypotheses, it is critical that the biophysical mechanisms underlying OB gamma oscillations be fully understood.

The mechanism of gamma oscillations in the OB is understood to be intrinsic to OB circuitry; gamma persists *in vivo* when cortical connections are severed [16–18] and it has been transiently evoked in OB slices *in vitro* [19–22]. Specifically, gamma oscillations depend upon reciprocal synaptic interactions between glutamatergic mitral cells (MCs) and GABAergic granule cells (GCs) within the OB external plexiform layer (EPL; [9], and reflect the quasi-periodic delivery of recurrent and lateral inhibition among MCs [19–21]. However, the dynamical mechanisms governing gamma oscillogenesis in the OB are not well understood. One common assumption has been that OB gamma is governed by a *pyramidal-interneuronal network gamma* (PING) mechanism; indeed, it bears some of the PING hallmarks, including reciprocal coupling of excitatory and inhibitory neurons and the substantial dependence of inhibitory GCs on input from excitatory MCs for their activation [23]. However, the theoretical stability of broadly coherent PING oscillations is challenged by the large heterogeneity in afferent input levels that is generated by normal odor stimulation and by the high level of uncoordinated background activity among MCs. Related network mechanisms also have been described that, while still based on MC/GC interactions, differ in diagnostic dynamical features – such as the oscillatory frequency depending on GABAergic synaptic latencies and rise times, rather than the decay time constant of the receptor [14]. An alternative model in which gamma oscillations are driven directly by intrinsic MC subthreshold oscillations (STOs), coupled but not governed by MC/GC synaptic interactions, also has been proposed [15]. MCs are known to exhibit distinctive STOs that influence the timing of action potentials and are phase-reset by inhibitory or shunting synaptic inputs [24,25]. This model demonstrates strong

synchronization of STOs (but not action potentials) among sparsely connected populations, but functions best in a nonspiking regime; in the model, mitral cell spikes and sparse granule cell spikes both challenge the stability of STO-driven gamma oscillations. However, STO-based mechanisms are better able to address the dynamical challenges posed by the imperfect synchronization of GC IPSPs (e.g., stochastic synchronization [26,27]).

To elucidate the mechanisms underlying gamma dynamics and intercolumnar coordination in the OB, we developed an OB slice preparation that exhibited persistent (minutes) gamma oscillations in response to the optogenetic excitation of OSN arbors or transient pharmacological stimulation with metabotropic glutamate receptor (mGluR) agonists, and recorded coherent local field potentials (LFPs) across 60 discrete electrodes using a planar multielectrode array (MEA). In sharp contrast to previous reports based on recordings from single electrodes [14,20], the blockade of GABA(A) receptors did not reduce oscillatory power in the gamma band. Rather, GABA(A) blockade decoupled neighboring areas of the OB, reducing the spatial extent of localized coherence, and modestly reduced the peak gamma frequency. The results could support a hybrid coupled oscillator mechanism in which the STOs of MCs across the OB are transiently synchronized by inhalation so as to quasi-synchronously excite GCs distributed broadly across the OB, some of which spike and perisomatically inhibit nearby MCs. This feedback inhibition constrains MC spike timing and perpetuates the gamma cycle via a PING-related network mechanism in which the synchronized inhibition from GCs recurrently resets MC STOs so as to impose the faster network frequency onto the network. Moreover, the recurrent quasi-

synchrony of GC spiking substantially enhances the theoretical stability of these PING-related field oscillations [23].

Materials and Methods

Mouse lines

For MEA recordings, we used male OMP-ChR2-EYFP (ORCM) transgenic mice[28] (provided by Venkatesh Murthy, Harvard University). This transgenic line coexpresses channelrhodopsin-2 (ChR2) and enhanced yellow fluorescent protein (EYFP) in olfactory sensory neurons (OSN) under the control of the olfactory marker protein (OMP) promoter, hence limiting transgene expression within the OB to OSN axon terminals in the glomerular layer (Figure 1.1a). Additional MEA experiments were performed with CD-1 outbred mice (Charles River, Kingston, NY, USA). All procedures for MEA experiments were performed under the auspices of a protocol approved by the Cornell University Institutional Animal Care and Use Committee (IACUC). Cornell University is accredited by The Association for Assessment and Accreditation of Laboratory Animal Care (AAALAC International).

Procedures for MEA recordings

OB slice preparation. Horizontal slices (300 um) were prepared from the olfactory bulbs of 28-42 day old mice. Mice were anesthetized with 2% isoflurane and ketamine (150 mg/kg ip), then decapitated, after which the olfactory bulbs were quickly removed. Slices were cut on a vibrating microtome (Integraslice 7550 PSDS) in an ice cold, oxygenated (with carbogen: 95% O2, 5% CO2), low-calcium/high-

Figure 1.1. MEA recordings from olfactory bulb slices. **(a)** 25um thick fixed OB slice from OMP-ChR2-EYFP transgenic mouse imaged with a fluorescent microscope (10x magnification) that shows the location of ChR2-EYFP coexpression limited to the glomerular layer. Inset with 20x magnification shows distinguishable glomeruli. **(b)** Single electrode recording from spontaneously firing MC/TC used to align slice to array. Inset shows 250ms of recording where multiple spike waveforms are present. Red overlay shows low-passed filtered data in the OB slice gamma band range (20-70 Hz). This "slice gamma" can be lower than classic gamma ranges. **(c)** Autocorrelation of 250 ms of filtered data (20-70 Hz; red) after three minutes following stimulation with 100 uM of the group I/II mGluR agonist ACPD compared to data taken 50 s prior to agonist application (black**).** Note the highly rhythmic ~40Hz oscillation. **(d)** Single-electrode spectrogram illustrating ACPD induced persistent, long lasting gamma oscillation. Time 0 indicates application of pharmacological agonist. Red arrow indicates time point of data shown in Figure 1.1c. **(e)** Automated gamma oscillation detection extracts high power regions of oscillations for array wide oscillation visulation and further analysis. Peak extractions are from spectrogram data in Figure 1.1d**.** See *Methods* for details. **(f)** MEA schematic overlaid to an OB slice shows a color coded representation of integrated LFP power (20-70Hz; hotter colors indicate regions of higher power) from 5 seconds of recording following stimulation with ACPD. The majority of gamma band activity occurs in the external plexiform layer (EPL) and adjacent mitral cell layer (MCL, *white dotted line*).

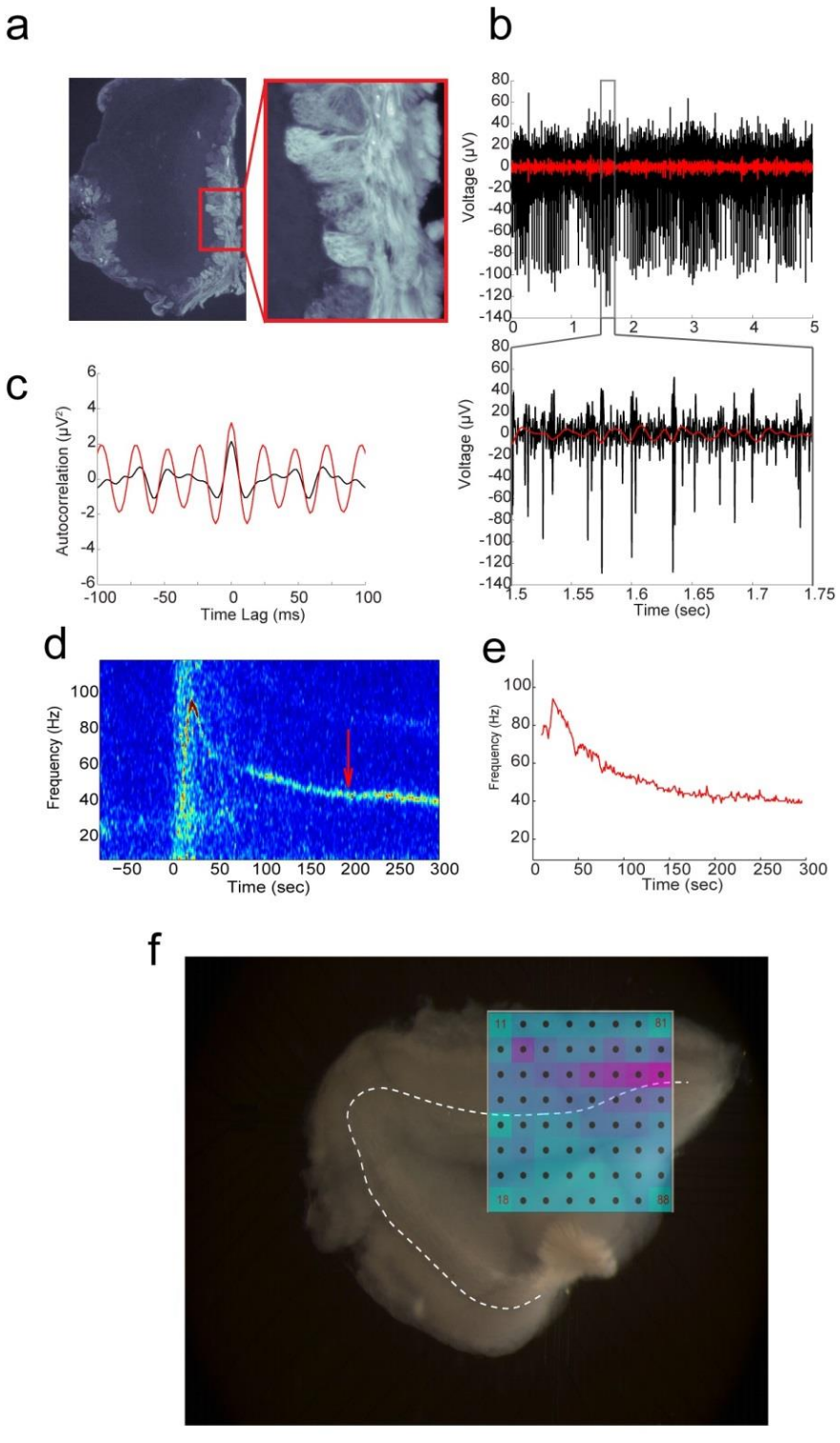
a
b
c
d
e
f
Voltage (μV)
Time (sec)
Autocorrelation (μV²)
Time Lag (ms)
Frequency (Hz)
Time (sec)
11
81
18
88

magnesium artificial cerebrospinal fluid (aCSF) dissection solution containing (in mM) NaCl 124, KCl 2.54, NaHCO3 26, NaH2PO4 1.23, CaCl2 1, MgSO4 3, glucose 10). Slices then were incubated in oxygenated dissection solution at 37°C for twenty minutes, and then maintained in oxygenated dissecting solution at room temperature until transfer to the recording well.

Electrophysiological recordings. During recordings, slices were continuously superfused at 1 mL/minute with heated (34°C), oxygenated aCSF (in mM: NaCl 125, KCl 3, NaHCO3 25, NaH2PO4 1.25, CaCl2 2, MgCl2 1, glucose 25) from a gravity-fed perfusion system. Slices were held in position by nylon webbing glued to a C-shaped chrome wire weight. Extracellular signals were recorded from OB slices using a 60-electrode planar microelectrode array (MEA; Multichannel Systems, Reutlingen, Germany). The array's 60 titanium nitride electrodes (30µm width, 30-50kΩ impedance) were arranged in an 8x8 grid (200µm pitch, minus the four corners; Figure 1.1f); electrode 15 (x-y coordinates of the array) was used as a reference. Each electrode on the MEA chip was individually connected to an amplifier in the MEA1060 baseplate. Signals were bandpass filtered (1Hz – 3000Hz), amplified (1200x gain), sampled (5-20 kHz at 16-bit resolution), and acquired using the vendor's MC_RACK software.

Pharmacology. Slices were stimulated by pipetting 100-125 uL of the appropriate pharmacological agent directly onto the slice in the recording well. Both the group I/II metabotropic glutamate receptor (mGluR) agonist 1-amino-1,3-dicarboxycyclopentane (ACPD) and the group I mGluR agonist 3,5-dihydroxyphenylglycine (DHPG) were used in these studies to evoke gamma oscillations. Both mGluR agonists yielded

similar results and are combined in analyses except where specified. Delivery of plain aCSF by pipet evoked no physiological responses, indicating that temperature or mechanical perturbations were not responsible for the observed effects.

The GABA(A) receptor antagonists bicuculline methiodide (BMI) and gabazine, and the GABA(B) receptor antagonist phaclofen, were generally bath-applied. However, when BMI was used to rescue gamma oscillations from suppression by phaclofen, BMI was delivered by pipette (1 mL) as described above. Gabazine blockade produced results similar to BMI blockade. All pharmacological agents were purchased from Sigma-Aldrich (St. Louis, MO, USA).

Additionally, while attempting to ensure that the failure of BMI application to block gamma oscillations was not due to the antagonist's inability to reach the recording sites on the underside of the slice, many slices were preincubated in BMI or gabazine prior to being placed in the recording chamber. Preincubation in BMI (50-100uM) or gabazine (500uM) had no greater effect than normal bath application (Figure S1.1).

Optical stimulation. A light engine (Lumencor, Beaverton, OR, USA) coupled to a light guide was used to stimulate OB slices from the OMP-EYFP-ChR2 transgenic mice. Slices were stimulated with 4Hz tetanic bursts of blue light (475nm) for 5 seconds with 15 mW/mm^2 of power.

Analysis of MEA data

General spectral processing. MEA recordings were resampled at 512 Hz and processed in Matlab. First, principal component analysis was performed on array-wide datasets to remove 60Hz interference and other highly correlated noise sources (PCA

denoising). Spectrograms then were computed with fast Fourier transforms (FFT) using 1 sec time intervals convolved with a triangular window. Intervals overlapped by 50% (i.e., 500 ms). The spectrograms were smoothed using a two-dimensional hamming window (16 points, 4 Hz by 4 sec). To extract LFP timeseries for further analysis, recordings were bandpass filtered with a 2nd order Butterworth filter (20Hz $\leq$ $f_{BP} \leq$ 70Hz). Biased autocorrelations were performed on 250 ms windows of bandpass-filtered data (Figure 1.1c).

Detection and extraction of gamma oscillations. The "slice gamma" band (20–70 Hz) extends to a lower frequency range than is customary for the gamma band *in vivo*. Oscillations across this full range are considered to reflect gamma within OB slices for functional reasons; *in vivo*, gamma oscillations are believed to be endogenous to the OB whereas functionally distinct beta-band oscillations in the OB require interactions with piriform cortex and would therefore not be observed in the isolated OB slice. To isolate persistent gamma oscillations induced in OB slices, we first thresholded spectrograms at two standard deviations above the mean gamma band power. This stringent criterion typically left small gaps in the gamma trace between clusters of putative gamma activity. These clusters were bridged via 1 standard deviation pixels, after which sufficiently large clusters (>5 sec) were identified as possible gamma oscillations. These clusters then were used as a mask on raw spectrograms for pathfinding. Beginning and end points were manually selected on the spectrogram, and the path between these points then was automatically plotted along the highest power pixels within the mask. Identified oscillations that exhibited a poststimulation shift in the peak power of the FFT and a stable peak frequency (<10 Hz variation for

80 sec; *analysis window*) were selected for analysis. When oscillatory frequencies are reported as X ± Y Hz, the uncertainty Y is the standard error of the mean

Analyses of power spectra. The frequency of LFP gamma oscillations within a given recording was determined by the mean peak frequency across an 80 second analysis window (Figure 1.2e-f). To assess the effects of optical stimulation or pharmacological manipulations on the integrated gamma band power, we compared 80 second analysis windows from before and after the manipulation. The gamma power (P_γ) was calculated by:

$$P_\gamma = \int_{20}^{55} X(f)\ df,$$

where *X(f)* is the FFT of the 80 second analysis window. Statistical significance was assessed using Student's t-test on the pre- and post-stimulus integrated gamma powers. Overlaid power spectra were computed with the same analysis windows using Welch's power spectral density estimate, after which the post-stimulus density (P_{post}) at frequency *f* was normalized to the pre-stimulus density (P_{pre}):

$$\Delta P(f)\% = \frac{P_{post}(f)}{P_{pre}(f)},$$

yielding $\Delta P(f)\%$, which is the percentage change in power density generated by the experimental manipulation (Figure 1.2c-d).

Analyses of coherence. Coherence (C_{xy}) between oscillations on two different electrodes was computed in the frequency domain via:

$$C_{xy}(f) = \frac{| < P_{xy}(f) >_n |}{\sqrt{< P_{xx}(f) >_n \cdot < P_{yy}(f) >_n}},$$

where P_{xx} and P_{yy} are autocorrelations and P_{xy} is the cross-correlation between the two electrodes, each averaged over n 1-sec epochs (here, n = 80). Note that C_{xy} is a complex number from which a magnitude and phase can be derived. Reference electrodes were selected from slices that had at least four adjacent electrodes with detectable, stable gamma band oscillations persisting for at least 80 second and a coherence magnitude ($|C_{xy}|$) of at least 0.15 across three neighboring electrodes. The frequency with the highest coherence magnitude (Figure 1.3a-b) was selected as the peak frequency (+/- 2 Hz) for that coherence group (of electrodes). For a given peak frequency, the electrode that had the greatest coherence magnitude with the largest number of neighboring electrodes was designated as the *reference electrode* for that coherence group. Pairwise coherence spectra then were calculated between each reference electrode and all other active electrodes from a given slice, and used to produce quiver plots (Figure 1.3c) and to calculate the average coherence across the spatial extent of the OB circuit (Figure 1.3d-e).

To assess the functional significance of coherence reductions observed under GABA(A) receptor antagonists, we sought to differentiate coherence arising from the synaptic coupling of neighboring OB columns from coherence arising simply from increased levels of (nonspecific) neuronal activity. To do this, we estimated the baseline level of nonspecific, activity-based ('spurious') coherence by scrambling the pairings of reference electrodes with their corresponding peak frequencies. Pairwise

coherence measurements then were made between each reference electrode and all other electrodes in the slice, producing a set coherence magnitudes identical to those of the nonscrambled condition but no longer constrained with respect to distance. This scrambling process therefore disrupts coherence arising from correlated activity among neighbors while preserving coherence arising from nonspecific activity. Comparing total coherence measurements against a baseline of spurious, nonspecific coherence measurements provides an estimate of the coherence that arises from correlated activity between neighboring electrode recordings.

Results

Persistent gamma oscillations are generated by optical stimulation of sensory neuron arbors or application of mGluR agonists

Horizontal slices of mouse olfactory bulb were laid onto a 60-channel planar microelectrode array (MEA; Multichannel Systems, Reutlingen, Germany) and aligned with the aid of endogenous spiking activity measured from the large pyramidal cells of the mitral cell layer (MCL; Figure 1.1b). No spiking activity was observed under these conditions from the glomerular layer or from layers deep to the MCL. Local field potentials recorded from the external plexiform layer (EPL) under control conditions in ACSF occasionally exhibited spectral peaks in the 20-70 Hz "slice gamma" band (henceforth *gamma band*; see *Methods*), but usually exhibited no stable peak frequencies prior to stimulation. Either optogenetic stimulation of channelrhodopsin-2 (ChR2)-expressing OSN axonal arbors within the glomerular layer (Figure 1.1a), or transient application of the Group I/II metabotropic glutamate

receptor (mGluR) agonist 1-amino-1,3-dicarboxycyclopentane (ACPD) induced persistent gamma band oscillations in the EPL that continued for several minutes (Figure 1.1c-f). To analyze these oscillations and their coherence across electrodes, we developed a method to identify and track the peak oscillatory power over time (Figure 1.1e; see *Methods*).

Oscillations recorded from neighboring MEA electrodes (200 um pitch) were independent, but often converged onto common stable gamma frequencies (Figure 1.2a-b). All spectral analyses performed herein were based on 80-second windows that began once all of the spectral peaks from electrodes recorded from a given slice had stabilized to consistent frequencies within a 10 Hz band (Figure 1.2a-b; *shaded region of spectrograms*). Both ChR2 stimulation and mGluR activation evoked strong spectral peaks in the gamma band compared to baseline activity (Figure 1.2c-d). Histograms of the mean peak frequencies from all recordings confirmed a relatively narrow peak among ChR2-activated slices (n=11 slices, 25 electrodes) and a broader, bimodally distributed set of peak frequencies in ACPD-activated slices (though any single electrode recording generally exhibited only a single dominant peak; n=11 slices, 52 electrodes) (Figure 1.2e-f). Gamma-band power was significantly increased by both ChR2 activation (paired t-test; $t(24) = 2.12$; $p < 0.05$) and ACPD activation ($t(51) = 4.44$; $p < 0.0001$); this increase was observable in nearly all recordings with optical stimulation (18/25 electrodes) and ACPD activation (50/52 electrodes) (Figure 1.2g-h).

Figure 1. 2. Gamma oscillations are recorded across multiple electrodes. **(a)** Recordings from seven MEA electrodes are overlaid from a single slice simultaneously exhibiting gamma oscillations following ChR2 stimulation. The electrode location for each trace is shown by the highlighted dots in the schematic of the MEA electrode layout (upper right). The highlighted segment of the gamma traces illustrates the 80-second quasi-steady-state oscillation data used in the data pool. Note that the seven oscillations converge onto two stable gamma frequencies rather than one (see below). **(b)** Same as (a) but following pharmacological stimulation by pipette application of 100 uL/100uM of the mGluR I/II agonist ACPD. Here the oscillations converge onto a single stable gamma frequency. Note that the induced oscillations persist long after the termination of optical stimulation (a) and washout of ACPD (b). **(c-d)** Overlaid average power spectra following (c) ChR2 activation (n = 11 slices/25 electrodes) and (d) ACPD stimulation (n = 11 slices/52 electrodes) with emergent power normalized to baseline spectral power at each frequency (see Methods). **(e-f)** Histogram showing the cumulative average frequency of the peak power from each 80 s traced oscillation induced by (e) ChR2 stimulation (n=25 electrodes) and (f) ACPD (n=52 electrodes). **(g-h)** Paired t-tests of the integrated gamma band range (20-55Hz) of the convergent freqency range identified by the cumulative average frequency historgrams (Figure e-f) show the (g) ChR2 stimulation ($t(24) = 2.12$; $p < 0.05$) and (h) ACPD ($t(51) = 4.44$; $p < 0.0001$) induced a significant increase in gamme band power compared to baseline integrated gamma power.

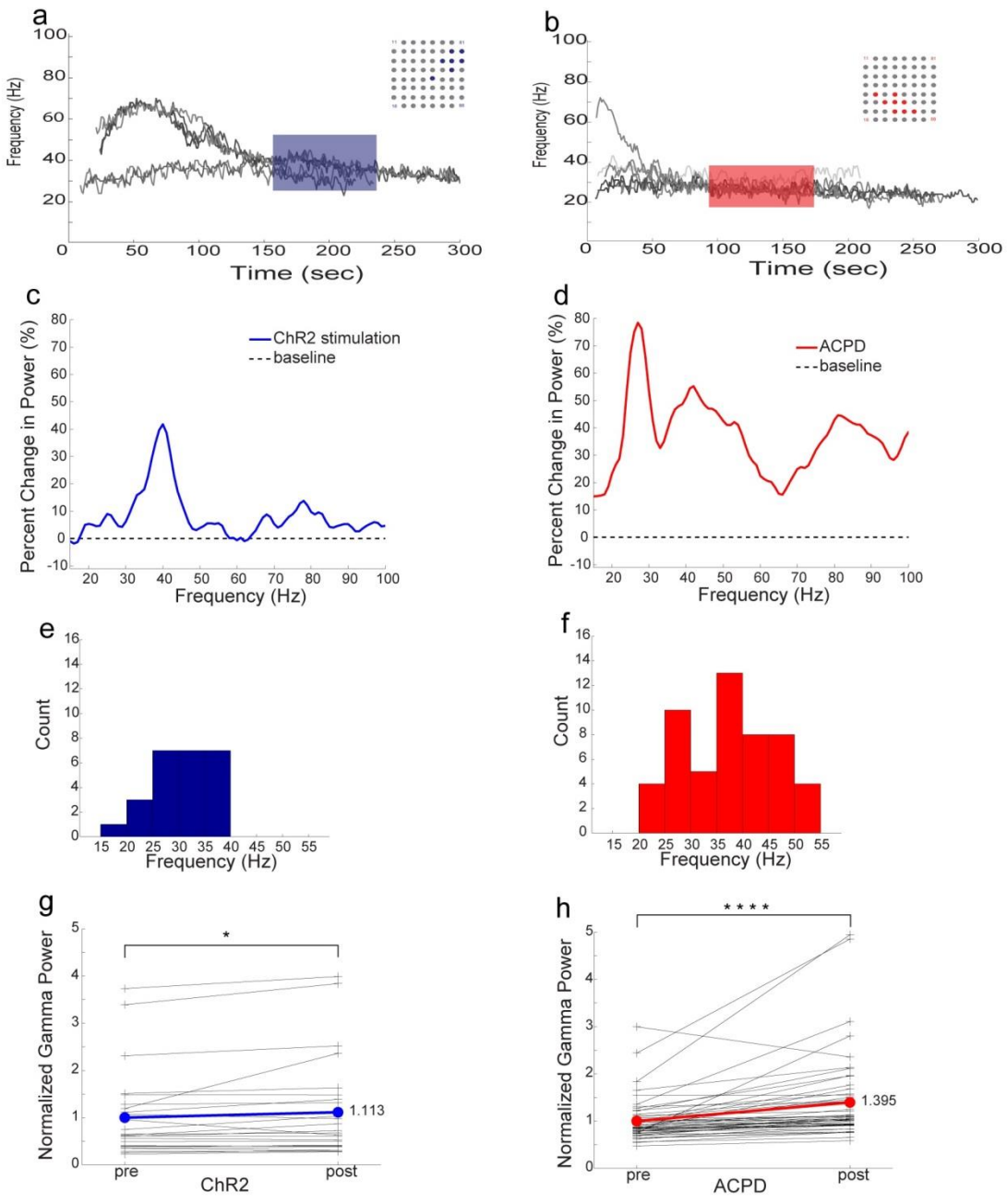
a
Frequency (Hz)
Time (sec)
b
Frequency (Hz)
Time (sec)
c
Percent Change in Power (%)
ChR2 stimulation
baseline
Frequency (Hz)
d
Percent Change in Power (%)
ACPD
baseline
Frequency (Hz)
e
Count
Frequency (Hz)
f
Count
Frequency (Hz)
g
Normalized Gamma Power
*
1.113
pre
post
ChR2
h
Normalized Gamma Power
****
1.395
pre
post
ACPD

Gamma oscillations form localized regions of coherence

Gamma oscillations often were coherent across multiple electrodes. To quantify the spatial patterns of coherence across the EPL, we selected each active electrode (i.e., exhibiting gamma-band activity) in turn and computed its coherence with all other such electrodes. For a given peak frequency, the electrode that had the greatest coherence magnitude with the largest number of neighboring electrodes was designated as the *reference electrode* for that coherence group. Pairwise coherence spectra then were calculated between each reference electrode and all other active electrodes from a given slice (Figure 1.3a-b). Notably, single OB slices could simultaneously exhibit multiple discrete localized patches of coherent gamma oscillations at different frequencies (Figure 1.3c). These results suggested that groups of neighboring OB columns were synchronized through synaptic interactions, with sharp discontinuities between local regions of coherence arising from the reduced density of lateral interactions produced by the slicing process – a phenomenon theoretically predicted by two-dimensional map-based models [29].

We measured the average spatial extent of coherent regions in slices by averaging the peak coherence magnitudes between reference electrodes and all electrodes (active or not) across all slices as a function of distance from the reference electrode. Both the optogenetic stimulation of ChR2-expressing OSN arbors (Figure 1.3d) and the transient application of mGluR agonists (Figure 1.3e) generated significant increases in gamma-band coherence across moderately distant electrodes compared to prestimulation coherence. Specifically, two-factor analysis of variance (ANOVA) for ChR2 data demonstrated highly significant effects of *stimulation*

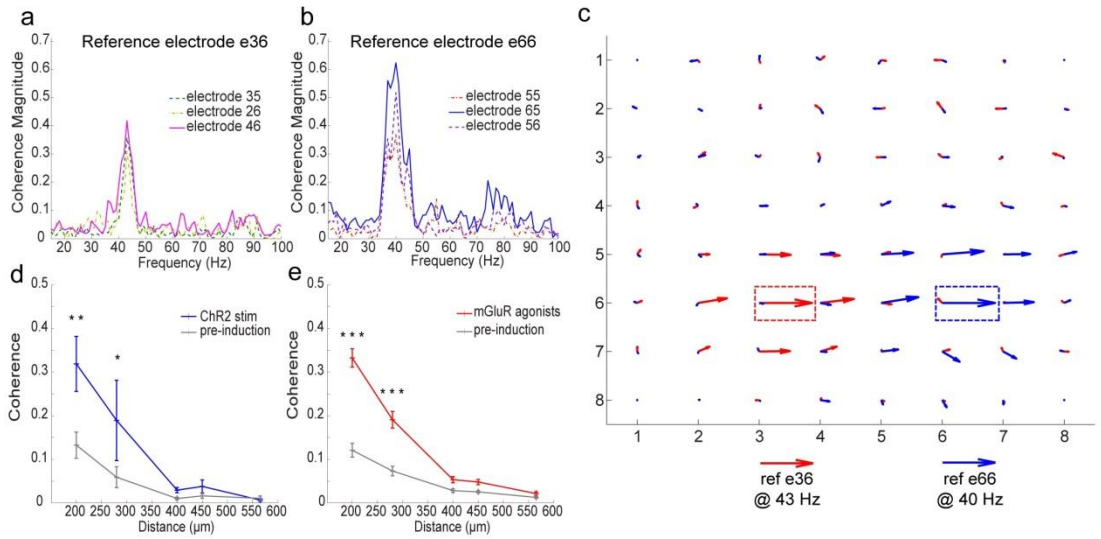

Figure 1.3. OB slices express multiple regions of coherent gamma oscillations. **(a)** Coherence between a selected reference electrode (e36; nomenclature based on x-y coordinates) and three adjacent electrodes. The frequency with the highest coherence magnitude in this region is 43 Hz. **(b)** Coherence between another reference electrode (e66) and three additional electrodes. The frequency with the highest coherence magnitude in this region is 40 Hz. **(c)** Quiver plot illustrating the simulataneous but adjacent pockets of coherence with reference electrode e36 (from Figure 1.3a,43 Hz, red arrows) and reference electrode e66 (from Figure 1.3b,40 Hz, blue arrows). The length of the arrows indicates coherence magnitude and the angle indicates phase. Note the nonoverlapping regions of independent coherence for each reference frequency. **(d)** Average coherence magnitude versus distance plot following ChR2 stimulation. Plot depicts the average coherence magnitude using 80s of stable-state data averaged across all adjacent electrodes (200 – 565 um distances) comparing pre vs post stimulation from multiple slices (n = 2 slices/2 reference electrodes; post hoc testing (simple main effects) 200 (p = 0.003) and 280 um (p = 0.026) distances). Error bars indicate SEM. **(e)** As in Figure 1.3d, but averaged coherence for mGluR agonist (Group I/II mGluR agonist ACPD and Group I mGlur agonist DHPG) application (n = 10 slices/15 electrodes; 200 and 280 um ($p < 0.001$) for both distances).

($F(1,60) = 7.467$, $p < 0.01$) and *distance* ($F(4,60) = 11.043$, $p < 0.001$); post hoc testing (simple main effects) indicated significant effects of ChR2 stimulation on coherence between electrodes at 200 ($p = 0.003$) and 280 um ($p = 0.026$) distances (Figure 1.3d). A similar analysis of the mGluR data revealed highly significant effects of both *stimulation* ($F(1,584) = 95.660$, $p < 0.001$) and *distance* ($F(4,584) = 108.524$, $p < 0.001$); post hoc tests indicated significant effects of mGluR stimulation on coherence at 200 and 280 um ($p < 0.001$ in both cases; Figure 1.3e). Coherence differences measured at distances above 400 um should not be interpreted as meaningful in any event, because the low absolute coherence values at these distances (roughly below 0.10) are reasonably likely to arise for spurious or artifactual reasons[30]. These localized regions of coherence in OB slices provide a uniquely rich preparation in which to study the construction and underlying mechanisms of spatial coherence in OB networks.

GABA(A) receptor blockade reduces the spatial coherence, not the power, of gamma oscillations

To test whether regional coherence arose from lateral inhibitory synaptic coupling, we bath-applied GABA(A) receptor antagonists and measured the resulting changes in gamma oscillatory power and regional coherence. Surprisingly, gamma-band oscillations persisted in the presence of saturating concentrations of GABA(A) receptor antagonists (Figure 1.4a) – a result seemingly at odds with other reports illustrating a strong sensitivity of OB gamma oscillations to GABA(A) blockade [14,20]. To explore this result, we computed the average power spectra from 22 electrodes

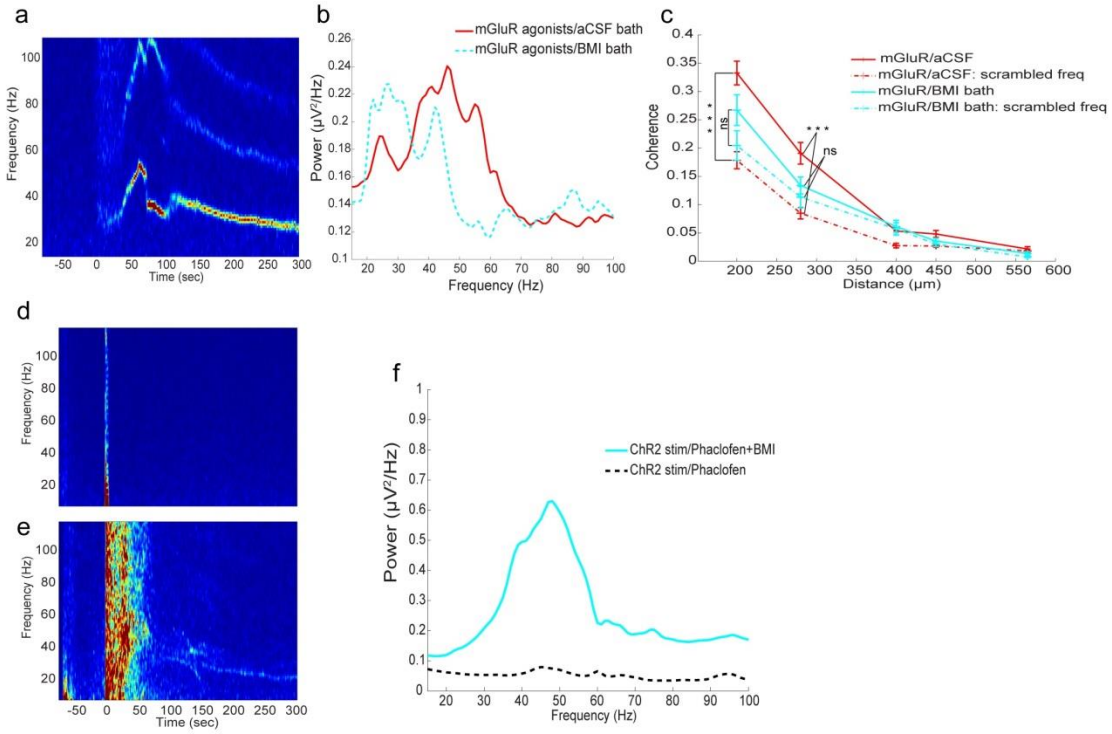

Figure 1.4. Intercolumnar synchronization is mediated by GABA(A) receptors, but local oscillations are GABA(A)-independent. **(a)** Spectrogram illustrates a long-lasting gamma band oscillation induced by mGluR agonists (Time 0) during continuous bath application of a GABA(A) receptor antagonist (50μM bicuculline methiodide, BMI). **(b)** Overlaid average power spectra comparing ACPD (100uM) and DHPG (125uM) induced oscillations in aCSF (red) to those in bath applied BMI (50-500μM; cyan). These data consisted of those oscillations that were recorded in both aCSF and BMI bath and persisted for 80s (22 electrodes/5 slices). Note the peak power shift to lower frequencies (46 to 27 Hz) along with the reduction of the average oscillation frequency (34 ± 2.15 Hz to 29 ± 1.19 Hz; paired t-test; $t(21) = 3.27$, $p<0.01$) produced by BMI bath application. **(c)** Comparison of oscillation coherence across space from mGluR agonist-induced oscillations in aCSF (solid line, *red*, same as Figure 1.3e) and during bath application of the GABA(A) receptor antagonist BMI (n = 3 slices/11 electrodes; 100-500 uM; solid line, *cyan*). To test for spurious coherence, the reference frequencies were scrambled between pairings of reference electrodes and their corresponding peak frequencies for both the aCSF and BMI data sets (broken lines; *red* and *cyan* respectively. Scrambling the reference frequencies significantly reduced the coherence across electrodes in aCSF (compare solid and broken *red* lines; Tukey HSD post hoc tests; 200 and 280 um; $p < 0.001$ in both cases), whereas the reduced coherence in the BMI bath was not significant (compare solid and broken *cyan* lines; $p > 0.40$ in all cases). **(d)** OB slice directly in bath with the GABA(B) antagonist (phaclofen, 100μM) reduced spontaneous activity and resulted in failure to elicit gamma band activity after ChR2 stimulation with light. The activity in the spectrogram at Time 0 is stimulus artifact. **(e)** BMI (500μM) pippeted directly on the OB slice in the phaclofen bath disinhibited bulbar networks and rescued gamma oscillations induced by 475nm light stimulation. **(f)** Averaged power spectra of light-induced oscillations (n = 4 slices/52 electrodes) in phaclofen bath (dashed line, *black*) and in phaclofen + BMI (solid line, *cyan*).

across 5 slices exposed to both control conditions and GABA(A) receptor blockade. Application of GABA(A) receptor antagonists did not significantly affect power in the gamma band, but did significantly reduce mean peak frequency (from 34 ± 2.15 Hz to 29 ± 1.19 Hz; paired *t*-test; t(21) = 3.27, $p < 0.01$; Figure 1.4b) and also reduced the sizes of spatially coherent regions (Figure 1.4c). To distinguish true coherence from baseline levels of spurious coherence as a result of an overall increase in activity following GABAergic blockade [30], we estimated the latter by scrambling the pairings of reference electrodes with their corresponding peak frequencies and calculating the average pairwise coherence from these scrambled data (Figure 1.4c, *dashed lines*; see *Methods*). Two-factor ANOVA demonstrated highly significant effects of *group* (F(7,1960) = 37.26; $p < 0.001$), *distance* (F(4,1960) = 282.242, $p < 0.001$), and the *group*distance* interaction (F(28,1960) = 9.783, $p < 0.001$); Tukey HSD post hoc tests comparing unscrambled to scrambled data indicated that under control conditions (mGluR agonists in aCSF), there was substantial true coherence among electrodes at 200 and 280 um distance ($p < 0.001$ in both cases), whereas when GABA(A) receptors were blocked with BMI, there was no significant true coherence between electrodes at any distance ($p > 0.40$ in all cases).

In the preceding experiments, to ensure that GABA(A) receptors were fully blocked, we applied the GABA(A) receptor antagonists bicuculline methiodide (BMI) (50-500 uM) or gabazine (500 uM; *data not shown*) at multiple (occasionally extreme) concentrations and sometimes preincubated slices in the antagonist within the recording chamber prior to positioning the holddown to ensure that the antagonists had access to the underside of the slice (Figure S1.1). However, it remained a possibility

that the persistent oscillations were a result of incomplete receptor blockade. To rule this out, we bath-applied the GABA(B) antagonist phaclofen (100 uM), which induces the broad release of GABA in the OB [31]. As expected, phaclofen application silenced all activity in the OB slice (Figure 1.4d). Coapplication of 500 uM BMI (delivered by pipette like the agonists) rescued the excitability of the slice and restored its ability to generate persistent gamma oscillations following ChR2 activation across many slices and electrodes (n = 4 slices/ 52 electrodes) (Figure 1.4e-f). These results indicate that localized (within-column) field oscillations are genuinely GABA(A) receptor-independent, and that these local oscillators can be coupled across multiple neighboring OB columns via GABA(A)-ergic synapses, generating broader regions of coherent activity.

Discussion

Our results indicate that local GABAergic feedback across the EPL underlies coherent gamma oscillations in the olfactory bulb but GABA(A) receptor activity does not govern local synchronization as evinced by persistent gamma band oscillations despite GABA(A) receptor blockade. When GABAergic activity was blocked, the gamma oscillations did exhibit a reduction in oscillation frequency but did not show a reduction in oscillation power indicating that other circuit mechanisms synchronize glomerular activity. GABA(A) receptor blockade did eliminate the gamma band coherence between oscillations recorded across multiple electrodes. We propose a hybrid coupled oscillator model of bulbar oscillogenesis in which synchronized MC STOs dictate local spike timing. The gamma oscillation frequency is largely

determined by repetitive inhibitory feedback from GABAergic granule cells that reset the STO phase imposing a faster network frequency. This GABAergic feedback across the EPL synchronizes the STOs effectively cohering intraglomerular synchronized activity across the OB producing coherent gamma oscillations.

The data presented here show that gamma band oscillations in slices of mouse olfactory bulbs can persist for many minutes. These are the first bulbar gamma oscillation recordings that show persistent oscillations (minutes) without repetitive stimulation [19,20]; Friedman and Strowbridge [19] showed increased field activity up to 60 minutes following 30 minutes of periodic stimulation every 45 seconds. The gamma oscillations in our study were induced by five seconds of 4 Hz (125 ms pulse duration) optical stimulation of OSN terminals that expressed ChR2; this stimulation produced long lasting activation of the bulbar circuitry. Transient pharmacological stimulation of metabotropic glutamate receptors also produced persistent gamma oscillations. These results further evince the robust, rhythmogenic characteristics of olfactory bulb circuitry when devoid of external cortical or sensory stimulation. Interestingly, these stimulation methods, tetanic stimulation of afferent inputs and application of metabotropic glutamate receptor agonists, have also been shown to induce gamma oscillation in hippocampal slices, indicating there may be conserved oscillogenic circuitry between the two structures (reviewed in [32]).

The recorded oscillations reached a quasi-stable frequency between 20-55 Hz, consistent with the 20-70Hz range recorded in other studies of gamma band synchronization in OB slices [14,19–21,26]. This lower band "slice gamma" is considered reflective of underlying synchronization circuitry due to the preservation of gamma

band power *in vivo* following the elimination of cortical feedback [16–18]. The observed frequency constraint of the recorded oscillations was not due to a temporal structure imposed by the stimulation paradigm. While the optical stimulation naturally contained a 4 Hz temporal structure, it should be noted that the induced oscillations continued long after the termination of optical stimulation and were at a much higher frequency than the stimulation. Similarly, the mGluR stimulation produced long lasting oscillations in the absence of temporally structured stimulation long after the agonists had washed out of the recording well.

Computational models of long range synchronization in cortical network models have predicted that a critical degree of connectedness between neural assemblies is necessary for fast synchronization [29]. Their results show that two-dimensional network models much more accurately reproduce the phase synchronization of gamma oscillations between long distance, oscillating regions of cortical areas. Our gamma oscillations recorded across multiple electrodes were coherent up to distances of 280 um, indicating that synchronization across multiple glomerular columns was present. Interestingly, multiple independent "pockets" of coherent oscillations were simultaneously recorded across OB slices. We interpret these results as indicative of reduced synaptic connectedness across the EPL that resulted from slicing the OB.. Indeed, GCs have been shown to have relatively local receptive fields in slices compared to their much larger receptive fields recorded in the intact OB *in vivo* where the EPL exhibits much denser connectivity[33]. A biophysically constrained computational model further supports the hypothesis that increasing the degree of connectedness from the estimated level of a slice up through the intact OB

leads to decreased "pockets" and increased overall coherence [33]. To further test this hypothesis, a viable experiment with OB slices would be to increase their thickness and calculate the average coherence magnitudes recorded across the OB slice (discussed in Chapter 2). Presumably, increasing the thickness of the slices, and therefore the connectedness across the EPL, would lead to increased coherence across oscillatory regions.

Gamma oscillations are observed in many areas across the brain and the best described theoretical network models (ING vs PING) are reliant upon inhibition; reviewed in [34]. Consistent with these predictions, other studies of gamma band synchronization in olfactory bulb slices show decreased gamma band power following GABA(A) receptor blockade [14,20]. Bathellier at al.[14], in particular, found that GABA(A) receptor blockade significantly reduced gamma band power, though this power was not completely abolished. Our results differ from these slice studies because GABA(A) blockade failed to block gamma oscillations and did decrease the frequency of the recorded oscillations. Our GABAergic application did, however, reduce the coherence across oscillating regions of the bulb. These results consequently can be explained by the difference between whether the recordings detected local synchronization or the spatially averaged gamma activity from desynchronized glomerular columns that would appear as a reduction in gamma band power. Our recording set-up with many channels positioned across the bulbar layers, specifically the EPL, is necessary to record local synchronization even though glomerular oscillations have been desynchronized due to GABA(A) receptor blockade. This was observed in our recordings by a failure to reduce gamma power with GABAergic

blockade but an elimination of coherence across interglomerular oscillations. A single extracellular electrode positioned near the MC layer, as described [14,20], would detect desynchronization amongst the frequency and phase of oscillators as a reduction in LFP power after spatial filtering across the extracellular space.

Our results suggest that GABA(A) receptor blockade decouples OB columns from one another, eliminating cross-columnar coherence and unmasking a slower, spatially localized, GABA(A) receptor-independent oscillatory mechanism. The slower peak frequency and the shrinking of coherent regions to areas consistent with a single glomerulus-associated column, in particular, both suggest that these GABA(A) receptor-independent oscillations are based on mitral cell STOs [15,24,25]. The STOs have slower oscillation frequencies, generally in the 15-35 Hz range, that are voltage dependent[24]. This frequency range is slower than traditional gamma but very similar to the oscillation frequencies we recorded during GABAergic blockade. These STOs are phasically reset by GABAergic feedback from GCs with the reset serving to synchronize STOs across the OB. Intact GABAergic synapses could serve to couple multiple columnar oscillators, as proposed by Brea et al.[15], but additionally increase the oscillatory frequency to a faster rhythm that depends on GABA(A) receptor kinetics. As GABAergic synaptic inhibition is able to reset the MC STO phase [24,25], this phenomenon is most parsimoniously modeled as an emergent PING-like network in which fast recurrent and lateral synaptic inhibition repeatedly and synchronously reset the phases of MC STOs, generating regional coherence across areas that are sufficiently densely synaptically coupled. In this framework, broad synchronous inhibition mediated by respiration-induced periglomerular cell activation initially

resets the STOs of activated MCs to a common phase, preparing the system for a rapid, STO-facilitated descent into PING-based coherent oscillations from which broad glomerular activation can be converted into a temporal metric for downstream computations.

REFERENCES

1. Womelsdorf, T. *et al.* Orientation selectivity and noise correlation in awake monkey area V1 are modulated by the gamma cycle. *Proc. Natl. Acad. Sci. U. S. A.* **109,** 4302–4307 (2012).

2. Vinck, M. *et al.* Gamma-phase shifting in awake monkey visual cortex. *J. Neurosci. Off. J. Soc. Neurosci.* **30,** 1250–1257 (2010).

3. Fries, P., Womelsdorf, T., Oostenveld, R. & Desimone, R. The effects of visual stimulation and selective visual attention on rhythmic neuronal synchronization in macaque area V4. *J. Neurosci. Off. J. Soc. Neurosci.* **28,** 4823–4835 (2008).

4. Kashiwadani, H., Sasaki, Y. F., Uchida, N. & Mori, K. Synchronized oscillatory discharges of mitral/tufted cells with different molecular receptive ranges in the rabbit olfactory bulb. *J. Neurophysiol.* **82,** 1786–1792 (1999).

5. Litaudon, P., Garcia, S. & Buonviso, N. Strong coupling between pyramidal cell activity and network oscillations in the olfactory cortex. *Neuroscience* **156,** 781–787 (2008).

6. Stopfer, M., Bhagavan, S., Smith, B. H. & Laurent, G. Impaired odour discrimination on desynchronization of odour-encoding neural assemblies. *Nature* **390,** 70–74 (1997).

7. Linster, C. & Cleland, T. A. Decorrelation of odor representations via spike timing-dependent plasticity. *Front. Comput. Neurosci.* **4,** 157 (2010).

8. Cleland, T. A. *et al.* Sequential mechanisms underlying concentration invariance in biological olfaction. *Front. Neuroengineering* **4,** 21 (2011).

9. Cleland, T. A. Construction of odor representations by olfactory bulb microcircuits. *Prog. Brain Res.* **208,** 177–203 (2014).

10. Fries, P. Neuronal gamma-band synchronization as a fundamental process in cortical computation. *Annu. Rev. Neurosci.* **32,** 209–224 (2009).

11. Freeman, W. J. Spatial properties of an EEG event in the olfactory bulb and cortex. *Electroencephalogr. Clin. Neurophysiol.* **44,** 586–605 (1978).

12. Kay, L. M. & Lazzara, P. How global are olfactory bulb oscillations? *J. Neurophysiol.* **104,** 1768–1773 (2010).

13. Fries, P. A mechanism for cognitive dynamics: neuronal communication through neuronal coherence. *Trends Cogn. Sci.* **9,** 474–480 (2005).

14. Bathellier, B., Lagier, S., Faure, P. & Lledo, P.-M. Circuit properties generating gamma oscillations in a network model of the olfactory bulb. *J. Neurophysiol.* **95,** 2678–2691 (2006).

15. Brea, J. N., Kay, L. M. & Kopell, N. J. Biophysical model for gamma rhythms in the olfactory bulb via subthreshold oscillations. *Proc. Natl. Acad. Sci.* **106,** 21954–21959 (2009).

16. Neville, K. R. & Haberly, L. B. Beta and gamma oscillations in the olfactory system of the urethane-anesthetized rat. *J. Neurophysiol.* **90,** 3921–3930 (2003).

17. Martin, C., Gervais, R., Chabaud, P., Messaoudi, B. & Ravel, N. Learning-induced modulation of oscillatory activities in the mammalian olfactory system: The role of the centrifugal fibres. *J. Physiol.-Paris* **98,** 467–478 (2004).

18. Martin, C., Gervais, R., Messaoudi, B. & Ravel, N. Learning-induced oscillatory activities correlated to odour recognition: a network activity. *Eur. J. Neurosci.* **23,** 1801–1810 (2006).

19. Friedman, D. & Strowbridge, B. W. Both electrical and chemical synapses mediate fast network oscillations in the olfactory bulb. *J. Neurophysiol.* **89,** 2601–2610 (2003).

20. Lagier, S., Carleton, A. & Lledo, P.-M. Interplay between local GABAergic interneurons and relay neurons generates gamma oscillations in the rat olfactory bulb. *J. Neurosci. Off. J. Soc. Neurosci.* **24,** 4382–4392 (2004).

21. Schoppa, N. E. Synchronization of olfactory bulb mitral cells by precisely timed inhibitory inputs. *Neuron* **49,** 271–283 (2006).

22. Gire, D. H. & Schoppa, N. E. Long-term enhancement of synchronized oscillations by adrenergic receptor activation in the olfactory bulb. *J. Neurophysiol.* **99,** 2021–2025 (2008).

23. Börgers, C. & Kopell, N. Effects of noisy drive on rhythms in networks of excitatory and inhibitory neurons. *Neural Comput.* **17,** 557–608 (2005).

24. Desmaisons, D., Vincent, J. D. & Lledo, P. M. Control of action potential timing by intrinsic subthreshold oscillations in olfactory bulb output neurons. *J. Neurosci. Off. J. Soc. Neurosci.* **19,** 10727–10737 (1999).

25. Rubin, D. B. & Cleland, T. A. Dynamical mechanisms of odor processing in olfactory bulb mitral cells. *J. Neurophysiol.* **96,** 555–568 (2006).

26. Galán, R. F., Fourcaud-Trocmé, N., Ermentrout, G. B. & Urban, N. N. Correlation-induced synchronization of oscillations in olfactory bulb neurons. *J. Neurosci. Off. J. Soc. Neurosci.* **26,** 3646–3655 (2006).

27. Ermentrout, B., Urban, N. & Galán, R. F. in *Coherent Behavior in Neuronal Networks* (eds. Josic, K., Rubin, J., Matias, M. & Romo, R.) 229–245 (Springer New York, 2009). at <http://link.springer.com/chapter/10.1007/978-1-4419-0389-1_12>

28. Dhawale, A. K., Hagiwara, A., Bhalla, U. S., Murthy, V. N. & Albeanu, D. F. Non-redundant odor coding by sister mitral cells revealed by light addressable glomeruli in the mouse. *Nat. Neurosci.* (2010). doi:10.1038/nn.2673

29. Bazhenov, M., Rulkov, N. F. & Timofeev, I. Effect of synaptic connectivity on long-range synchronization of fast cortical oscillations. *J. Neurophysiol.* **100,** 1562–1575 (2008).

30. Buzsáki, G. & Schomburg, E. W. What does gamma coherence tell us about inter-regional neural communication? *Nat. Neurosci.* **18,** 484–489 (2015).

31. Isaacson, J. S. & Vitten, H. GABA(B) receptors inhibit dendrodendritic transmission in the rat olfactory bulb. *J. Neurosci. Off. J. Soc. Neurosci.* **23,** 2032–2039 (2003).

32. Whittington, M. A., Traub, R. D., Kopell, N., Ermentrout, B. & Buhl, E. H. Inhibition-based rhythms: experimental and mathematical observations on network dynamics. *Int. J. Psychophysiol. Off. J. Int. Organ. Psychophysiol.* **38,** 315–336 (2000).

33. Peace, S. T. *et al.* Hybrid coupled-oscillator mechanism generates coherent gamma oscillations in olfactory bulb slices. (in preparation).

34. Buzsáki, G. & Wang, X.-J. Mechanisms of gamma oscillations. *Annu. Rev. Neurosci.* **35,** 203–225 (2012).

Appendix 1.1. Supplementary figure.

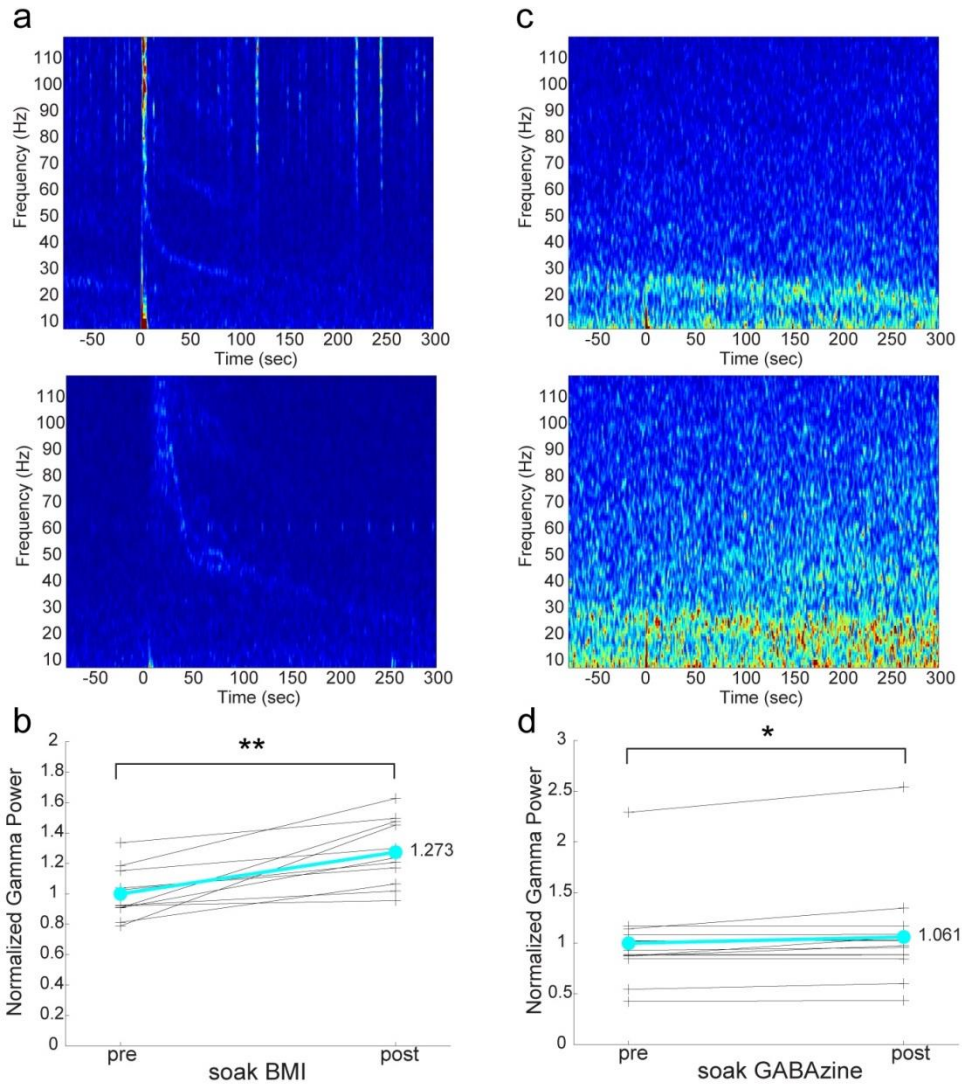

Figure S1.1. Soaking OB slices in GABA(A) receptor antagonists failed to block gamma activity. **(a)** Two spectrograms show gamma band activity is induced by DHPG following soaking slices in GABA(A) receptor antagonists. **(b)** Paired t-tests show there was a significant increase in integrated gamma band power (20-55Hz) compared to prestimulus integrated power (n=2 slices/ 11 electrodes; $t(10) = 4.44$; $p < 0.01$) despite GABAergic blockade in multiple concentrations of GABA(A) receptor antagonist bicuculline methiodide (BMI; 50-100 uM). **(c)** Two spectrograms show enhanced gamma band power after optical stimulation of ChR2 following soaking slices in 500 uM gabazine. **(d)** Paired t-tests show significant increase in integrated gamma band power (20-55Hz) compared to prestimulus integrated power (n = 2 slices/14 electrodes; $t(13) = 2.58$; $p < 0.05$).

CHAPTER 2

BROAD DIMENSIONAL CONNECTIVITY FACILITATES COHERENT GAMMA OSCILLATIONS IN THE OLFACTORY BULB

Shane T. Peace[1*], Benjamin C. Johnson[2], Alyosha C. Molnar[2], Thomas A. Cleland[3*]

[1]Dept. Neurobiology & Behavior

[2]Dept. Electrical and Computer Engineering

[3]Dept. Psychology

Cornell University

Ithaca, NY 14853

Introduction

Gamma oscillations, recorded in the 30-80 Hz range of the local field potential (LFP), indicate synchronization amongst coactivated neural populations. These oscillations are thought to underlie a multitude of neural functions – e.g., cortical sensorimotor integration[1], binding the disparate features of visual objects[2], and the routing of hippocampal place cell information[3]. Coherent gamma oscillations across the rodent olfactory bulb (OB) are a conspicuous trademark of bulbar recordings during odor investigation[4,5] with increased gamma power emerging during increased task demands[6]. In the insect antennal lobe, disruption of 20-35 Hz LFP oscillations, analogous to rodent gamma oscillations, caused increased generalization between responses to similar odorants while preserving the overall firing rates and response profiles of projection neurons[7,8]. These data suggest that gamma band synchronization is critical for high-resolution odorant constructions; therefore, it is important to further clarify the bulbar circuitry that generates these biophysical gating mechanisms.

Despite the prominence of gamma oscillations across the brain, the local circuitry that underlies this rhythmic activity continues to be an active area of research. In the olfactory bulb, gamma oscillations are thought to be intrinsic to bulbar circuitry[9–11] and are hypothesized to rely on excitatory-inhibitory synaptic interactions in the external plexiform layer (EPL) between the glutamatergic mitral cells (MC) and the GABAergic granule cells (GCs)[10,12]. This interaction between excitatory and inhibitory cells is similar to the pyramidal-interneuron network gamma (PING) hypothesis of cortical gamma oscillations that necessarily relies upon feedback inhibition to synchronize the excitatory spike driver currents. Contrary to these

predictions, OB gamma oscillations have been shown to persist despite GABAergic blockade in recordings from awake-behaving mice[13] and in OB slice recordings (Chapter 1); therefore, a demand persists for further refined hypotheses of gamma oscillogenesis in the olfactory bulb.

An alternate model of gamma band rhythmogenesis, independent of the GABA(A) inhibition mediated time constant, emphasizes MC membrane voltage subthreshold oscillations (STOs)[14] as a plausible mechanism underlying gamma range synchronization. In this model, the STO phases constrain MC spike times directly; GABAergic feedback from GCs functions to synchronize the STOs but not to directly regulate MC spike timing [15,16]. In this model, oscillations across the OB, due to individual mitral cell STOs, are synchronized by long range interactions between mitral and granule cells[17]. Therefore, the degree of dendrodendritic connectivity across the EPL appears to be a critical component of synchronizing gamma oscillations across the glomerular columns of the OB. Indeed, reducing the long range connectivity between mitral and granule cells by slicing has resulted in isolated pockets of parallel coherent activity across OB slices (Chapter 1, Figure 1.3c). Furthermore, blocking GABA(A) receptors did not block local synchronization but did reduce the coherence of oscillating regions by preventing feedback inhibition from GCs. Here, we test to what extend long-range interactions between MCs and GCs effect coherent oscillations by manipulating the dimensionality of connectedness across the EPL by varying the thickness of OB slices.

To investigate the role of long range interactions for coherent gamma oscillations across multiple glomerular columns, we developed a slice preparation of

the mouse OB from which we recorded spatially broad local field potentials (LFPs) using a 60-channel planar, microelectrode array (MEA, MultiChannel Systems). Similar to recordings from slices of the hippocampus[18,19], we found that the non-specific cholinergic agonist carbachol successfully induced long-lasting (minutes) gamma oscillations across the EPL. These oscillations showed levels of coherence quantitatively similar to previously reported OB gamma oscillations produced by optical stimulation of OSN arbors expressing channelrhodopsin-2 (ChR2) or chemical stimulation with metabotropic glutamate receptor (mGluR) agonists (Chapter 1).

To measure the influence that EPL connectivity has on bulbar synchronization, we recorded carbachol-induced gamma oscillations from OB slices of two different thicknesses: 300 and 400um. If dense GABAergic feedback from GCs in the EPL does indeed help coordinate oscillatory activity across glomerular columns, then we expect increasing this density by taking thicker slices will increase the coherence of gamma oscillations recorded across the OB slices. Interestingly, increasing the thickness of the OB slice did produce increased coherence across oscillating regions of the EPL. Blockade of GABA(A) receptors failed to block gamma band oscillations, but reduced oscillatory coherence, consistent with our previously reported data (Chapter 1). GABA(A) receptor antagonist application to the thicker slices reduced oscillation coherence to similar values previously recorded in slices stimulated by metabotropic glutamate receptor agonists in the presence of GABA(A) receptor antagonists (Chapter 1, Figure 1.4c). These results further demonstrate that bulbar coherence is mediated by lateral inhibitory feedback by GABAergic synapses onto mitral cells.

Materials and Methods

For MEA recordings, we used male OMP-ChR2-EYFP (ORCM) transgenic mice (provided by Venkatesh Murthy, Harvard University). For these experiments, we did not optically stimulate the channelrhodopsin-2 (ChR2). All procedures for MEA experiments were performed under the auspices of a protocol approved by the Cornell University Institutional Animal Care and Use Committee (IACUC). Cornell University is accredited by The Association for Assessment and Accreditation of Laboratory Animal Care (AAALAC International).

OB slice preparation. Horizontal slices (300 or 400 um) were prepared from the olfactory bulbs of 28-42 day old mice. Mice were anesthetized with 2% isoflurane and ketamine (150 mg/kg ip), then decapitated, after which the olfactory bulbs were quickly removed. Slices were cut on a vibrating microtome (Integraslice 7550 PSDS) in an ice cold, oxygenated (with carbogen: 95% O2, 5% CO2), low-calcium/high-magnesium artificial cerebrospinal fluid (aCSF) dissection solution containing (in mM) NaCl 124, KCl 2.54, NaHCO3 26, NaH2PO4 1.23, CaCl2 1, MgSO4 3, glucose 10). Slices were incubated in oxygenated dissection solution at 37°C for twenty minutes, and then maintained in oxygenated dissecting solution at room temperature until transfer to the recording well.

Electrophysiological recordings. During recordings, slices were continuously superfused at 1 mL/minute with heated (34°C), oxygenated aCSF (in mM: NaCl 125, KCl 3, NaHCO3 25, NaH2PO4 1.25, CaCl2 2, MgCl2 1, glucose 25) from a gravity-fed perfusion system. Slices were held in position by nylon webbing glued to a C-shaped chrome wire weight. Extracellular signals were recorded from OB slices using

a 60-electrode planar microelectrode array (MEA; Multichannel Systems, Reutlingen, Germany). The array's 60 titanium nitride electrodes (30µm width, 30-50kΩ impedance) were arranged in an 8x8 grid (200µm pitch, minus the four corners; Figure 2.1b,d); electrode 15 (x-y coordinates of the array) was used as a reference. Each electrode on the MEA chip was individually connected to an amplifier in the MEA1060 baseplate. Signals were bandpass filtered (1Hz – 3000Hz), amplified (1200x gain), sampled (10 kHz at 16-bit resolution), and acquired using the vendor's MC_RACK software.

Pharmacology. Slices were stimulated by pipetting 100 uL of the nicotinic and muscarinic acetylcholine agonist carbachol directly onto the slice in the recording well. Notably, these agents diluted and washed out rapidly, indicating that the oscillogenic effects of these agents long outlasted their presence in the bath. This rapid washout was confirmed by the timed evacuation of food coloring added to aCSF line that flowed into the recording well. All noticeable food coloring was absent within 60 seconds. The GABA(A) receptor antagonist bicuculline methiodide (BMI; 200uM) was bath applied to the slice. All pharmacological agents were purchased from Sigma-Aldrich (St. Louis, MO, USA).

General spectral processing. MEA recordings were resampled at 512 Hz and processed in Matlab. First, principal component analysis was performed on array-wide datasets to remove 60Hz interference and other highly correlated noise sources (PCA denoising). Spectrograms then were computed with fast Fourier transforms (FFT) using 1 second time intervals convolved with a triangular window (Figure 2.1e). Intervals overlapped by 50% (i.e., 500 ms). The spectrograms were smoothed using a

two-dimensional hamming window (16 points, 4 Hz by 4 second).

Detection and extraction of gamma oscillations. The "slice gamma" band (20–70 Hz) extends to a lower frequency range than is customary for the gamma band *in vivo*. To isolate persistent gamma oscillations induced in OB slices, we first thresholded spectrograms at two standard deviations above the mean gamma band power. This stringent criterion typically left small gaps in the gamma trace between clusters of putative gamma activity. These clusters were bridged via 1 standard deviation pixels, after which sufficiently large clusters (>5 sec) were identified as possible gamma oscillations (Figure 2.1f). These clusters then were used as a mask on raw spectrograms for pathfinding. Beginning and end points were manually selected on the spectrogram, and the path between these points then was automatically plotted along the highest power pixels within the mask (Figure 2.1g). Identified oscillations that exhibited a poststimulation shift in the peak power of the FFT and a stable peak frequency (<10 Hz variation for 80 sec; *analysis window*) were selected for analysis. When oscillatory frequencies are reported as X ± Y Hz, the uncertainty Y is the standard error of the mean.

Analyses of power spectra. The frequency of LFP gamma oscillations within a given recording was determined by the mean peak frequency across an 80 second analysis window (Figure 2.2c). To assess the effects of pharmacological manipulations on the integrated gamma band power, we compared 80 second analysis windows from before and after the manipulation. The gamma power (P_γ) was calculated by:

$$P_\gamma = \int_{20}^{55} X(f)\, df.$$

where *X(f)* is the FFT of the 80 second analysis window. Statistical significance was assessed using Student's t-test on the pre- and post-stimulus integrated gamma powers. Overlaid power spectra were computed with the same analysis windows using Welch's power spectral density estimate, after which the post-stimulus density (P_{post}) at frequency *f* was normalized to the pre-stimulus density (P_{pre}):

$$\Delta P(f)\% = \frac{P_{post}(f)}{P_{pre}(f)},$$

yielding $\Delta P(f)\%$, which is the percentage change in power density generated by the experimental manipulation (Figure 2.2b).

Analyses of coherence. Coherence (C_{xy}) between oscillations on two different electrodes was computed in the frequency domain via:

$$C_{xy}(f) = \frac{|< P_{xy}(f) >_n|}{\sqrt{< P_{xx}(f) >_n \cdot < P_{yy}(f) >_n}},$$

where P_{xx} and P_{yy} are autocorrelations and P_{xy} is the cross-correlation between the two electrodes, each averaged over *n* 1-second epochs (here, *n* = 80). Note that C_{xy} is a complex number from which a magnitude and phase can be derived. Reference electrodes were selected from slices that had at least four adjacent electrodes with detectable, stable gamma band oscillations persisting for at least 80 seconds and a coherence magnitude ($|C_{xy}|$) of at least 0.15 across three neighboring electrodes. The frequency with the highest coherence magnitude (Chapter 1 - Figure 1.3a-b) was

selected as the peak frequency (+/- 2 Hz) for that coherence group of electrodes. For a given peak frequency, the electrode that had the greatest coherence magnitude with the largest number of neighboring electrodes was designated as the *reference electrode* for that coherence group. Pairwise coherence spectra then were calculated between each reference electrode and all other active electrodes from a given slice, and used to produce quiver plots (Figure 2.3c-d) and to calculate the average coherence across the spatial extent of the OB circuit (Figure 2.3e-f). To discriminate between real and spurious coherence, we scrambled the coupling between reference electrodes and the optimal coherence frequency as described in more detail in Chapter 1 *Methods.*

Results

Cholinergic agonists induce persistent gamma band synchronization across OB slices.

Horizontal slices of mouse olfactory bulbs were laid onto a 60-channel planar microelectrode array (MEA; Multichannel Systems, Reutlingen, Germany) and aligned with the aid of endogenous spiking activity from the large mitral cells (MCs) of the mitral cell layer (Figure 2.1a). OB layer identification was performed following experiments by plotting the integrated spike power range (filtered between 200 – 3000 Hz) for all sixty electrodes. The spiking range power was constrained to the mitral cell layer and across the external plexiform layer (EPL) with no spiking power in the glomerular or granule cell layer (Figure 2.1a-b). Local field potentials (LFP) recorded prior to stimulation in aCSF showed unstable, transient spectral power in the slice

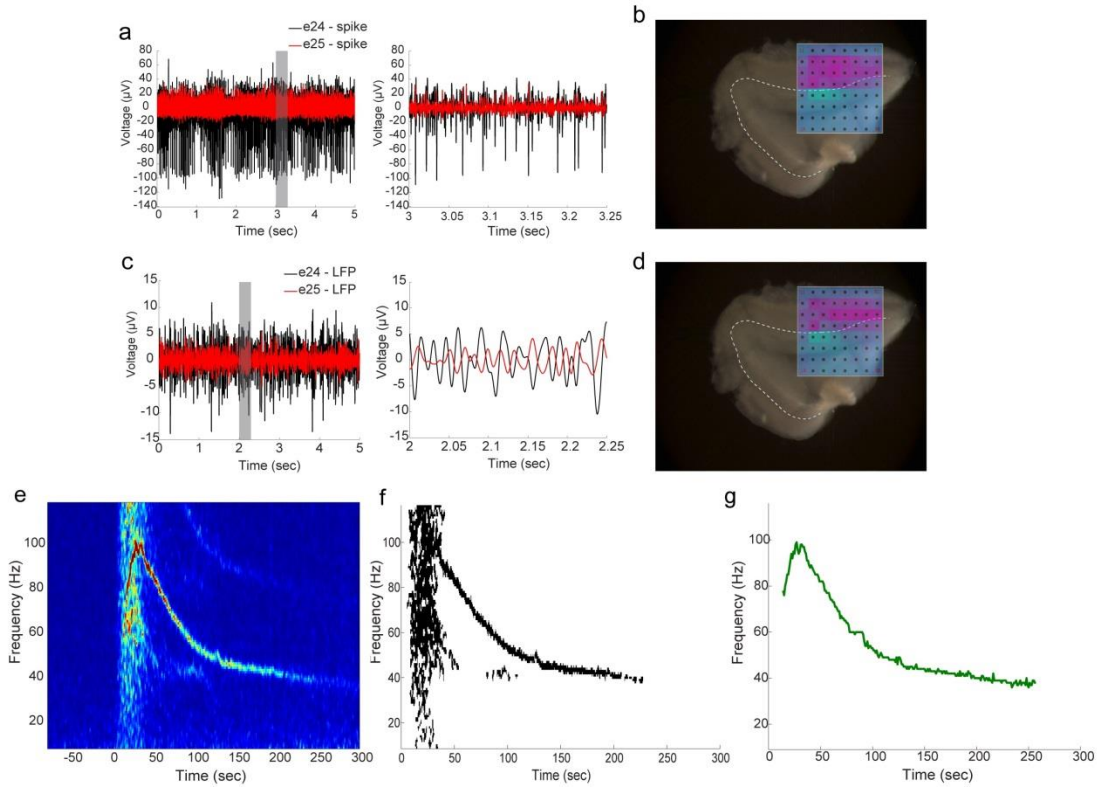

Figure 2.1. MEA recordings from OB slices. **(a)** Single electrode (e24, black trace) recording of spontaneous activity near the MC layer from multiple units (5 second trace) with multiple AP waveforms clearly distinguishable (inset; indicated by shaded area of **a**-left). An adjacent electrode (e25, red trace) in the granule cell layer does not record spiking activity. **(b)** The MEA schematic overlay shows a color coded representation (pink equals more activity) of integrated action potential band power (200-3000Hz) from 5 seconds of recording from an OB slice. The spiking power band was associated with the MC layer (white dotted line) and extended into the EPL **(c)**. Band passed data (20-70Hz) from e24 (black trace) shows more gamma band activity than adjacent e25 (red trace) that is recording from the GC layer. Inset shows 250ms of data indicated by grey trace in Figure 2.1**c**-left. **(d)** The integrated gamma band power overlay (20-70Hz) shows the majority of gamma band activity occurs in the MC/EPL. Note the regional overlap between spiking and gamma band activity. **(e)** Single-electrode spectrogram illustrating carbachol (186uM) induced persistent, long lasting gamma oscillation. Time 0 indicates application of pharmacological agonist. **(f)** single-electrode oscillation detection from spectogram data Figure 2.1e are power threshold filtered and remaining pixel clusters are joined allowing for semi-blind, oscillation detection **(g)** Automated gamma oscillation tracing extracts high power regions of oscillations for array wide oscillation visulation and further analysis. Peak extractions are from spectrogram data in Figure 2.1e. See *Methods* for details

gamma band (20 – 70 Hz; termed *gamma band*) across the mitral cell layer and EPL (Figure 2.1c-d). OB slice regions that exhibited gamma range activity overlapped with bulbar spiking activity. Pipette application of the nicotinic and muscarinic acetylcholine receptor agonist carbamoylcholine chloride (carbachol) produced persistent (up to 5 minutes), stable gamma band oscillations across the EPL as viewed by plotting spectrograms of low passed, LFP data from single electrodes (Figure 2.1e) High power spectral activity in the plotted spectrograms that met duration and power thresholds (Figure 2.1f; see *Methods*) were detected by a custom Matlab program designed to identify persistent gamma synchronization. The peak power of the detected oscillations in the spectrograms were traced and extracted for oscillation quantification and visualization with other recorded oscillations (Figure 2.1g; see *Methods*).

Carbachol induced multiple, independent oscillations across the OB slices that were recorded by separate electrodes (200um pitch), but exhibited convergence onto common gamma band frequencies (Figure 2.2a). The oscillation traces were recorded from adjacent electrodes illustrated by the MEA schematic in the upper right hand corner of the figure. All further spectral analyses were performed on 80-second windows that began once all of the spectral peaks from oscillations across a given slice had stabilized onto consistent frequencies (within a 10 Hz band) illustrated by the highlighted portion of the traced spectrogram (Figure 2.2a). Carbachol induced tightly constrained gamma oscillations as seen in the averaged FFT analysis (see *Methods*) of the carbachol data (n = 6 slices/20 electrodes) that shows a sharp peak in the gamma band (centered at 41 Hz) compared to mean baseline activity (Figure 2.2b). The mean

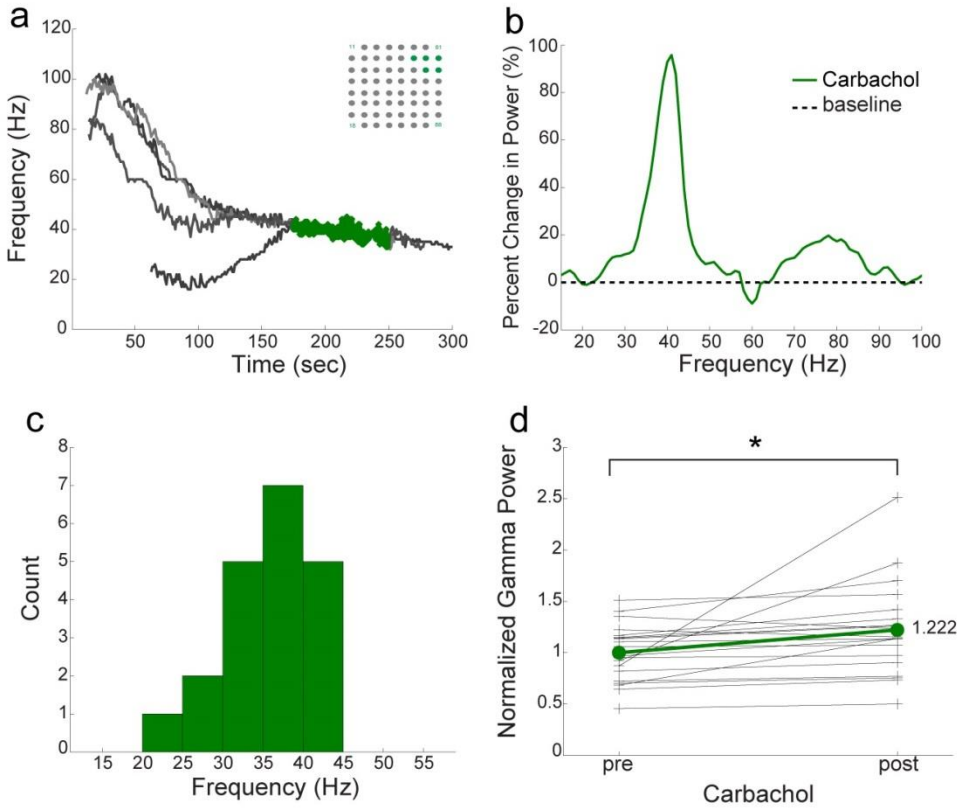

Figure 2.2. Gamma oscillations are recorded across multiple electrodes. **(a)** Recordings from five MEA electrodes are overlaid from a single slice simultaneously exhibiting gamma oscillations following carbachol stimulation. The electrode location for each trace is shown by the highlighted dots in the schematic of the MEA electrode layout (upper right). The highlighted segment of the gamma traces illustrates the 80-second quasi-steady-state oscillation data used in the data pool. **(b)** Overlaid average power spectra following carbachol application (n = 6 slices/20 electrodes) with emergent power normalized to baseline spectral power at each frequency (see Methods). **(c)** Histogram showing the cumulative average frequency of the peak power from each 80 s traced oscillation induced by carbachol (n = 20). **(d)** Paired t-tests of the integrated gamma band (20-55Hz; defined by Chapter 1,Figure 1.2 e-f) of the convergent freqency data show the carbachol induced a significant increase in gamma band power ($t(19) = 2.46$; $p < 0.05$) compared to baseline integrated gamma power.

frequency histogram of the peak oscillation power further details the precise oscillatory rhythm evoked by the broad cholinergic agonist showing the majority of oscillations had an average frequency that mirrored the spectral power distribution (mean 35.7 ± 1.14 Hz) (Figure 2.2c). The induced gamma band oscillatory power integrated between 20-55Hz was significant compared to integrated baseline activity (paired t-test $t(19) = 2.46$; $p < 0.05$) (Figure 2.2d). These results indicate that activation of cholinergic receptors across OB slice produces persistent, tightly constrained gamma oscillations. This stimulation of gamma band oscillations across multiple regions of the OB slice allowed us to further investigate the bulbar circuitry underlying coherent gamma oscillations shown to exist in the intact OB of rodents

Increased bulbar connectedness produced greater coherence amongst gamma oscillations.

We tested the hypothesis that increased EPL connectedness would increase coherence between evoked gamma oscillations. Gamma oscillations evoked by carbachol were moderately coherent across OB slices with most slices exhibiting oscillations across multiple electrodes. We quantified coherence across oscillations in the EPL by pairing oscillation frequency with the electrode that had the highest coherence magnitude (termed *oscillation reference* electrode) across neighboring electrodes recording the same oscillation (see *Methods*). Pairwise calculations were made between the reference electrode and surrounding electrodes at 200, 280, 400, 450, and 565 um away. It is unclear from these data whether an increase of 100 um to the OB slice thickness increased the spatial spread of coherent LFPs (Figure 2.3a-b).

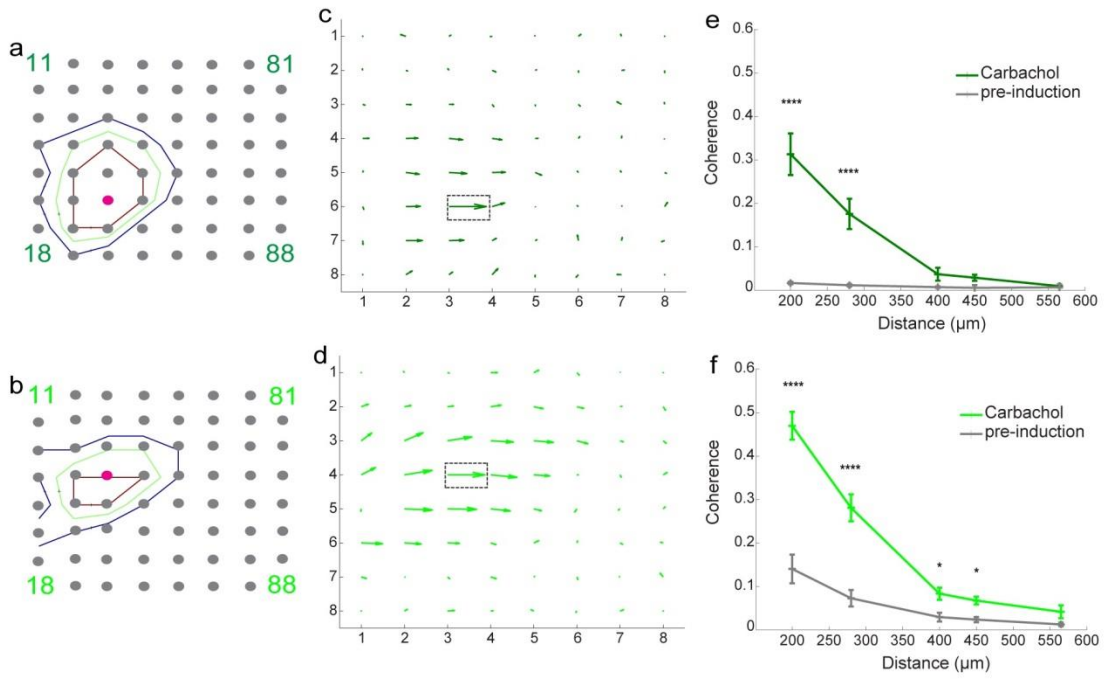

Figure 2.3. Thicker slices produce increased coherence magnitude. **(a)** Typical coherence magnitude from single 300um thick slice showing standard deviation spread of coherence values across MEA schematic. Red electrode represents reference electrode with blue rings equal to 1 s.d. above the mean, green ring equal to 2 s.d. and red ring equal to 3 s.d. compared to prestimulation baseline. **(b)** Same as in Figure 2.3a but with 400um thick slices. Note that the increased slice thickness does not produce substantially larger regions of coherence. **(c)** Quiver plot of data in Figure 2.3a. The length of the arrows indicates coherence magnitude and the angle indicates phase. These data are used to calculate the average coherence magnitude across the discrete electrode distances. **(d)** Same as in Figure 2.3c but with 400um thick slices. These data show increased coherence magnitude across oscillating regions as a result of thicker slices. **(e)** Average coherence magnitude versus distance plot following carbachol stimulation. Plot depicts the average coherence magnitude using 80s of stable-state data averaged across all adjacent electrodes (200 – 565 um distances) comparing pre vs post stimulation from multiple slices (n = 3 slices/4 reference electrodes); post hoc testing (simple main effects) 200 and 280um ($p<0.0001$ for both) Error bars indicate SEM. **(f)** Same as in Figure 2.3e, but with 400um thick slices. Pre vs post stimulation from multiple slices (n = 3 slices/ 6 reference electrodes); post hoc testing (simple main effects) 200,280 um ($p<0.0001$) and 400,450 um ($p<0.05$) distances.

The coherence values of the oscillations were increased, however, as viewed by a comparison of quiver plots from a 300um (Figure 2.3c) and a 400um (Figure 2.3d) thick slice. The length of the arrows indicates coherence magnitude and the arrow angle indicates the phase relationship to the reference electrode (boxed arrow). Carbachol significantly increased gamma oscillation coherence across moderately distant electrodes (Figure 2.3e) compared to prestimulation coherence. More specifically, three-factor analysis of variance (ANOVA) for carbachol *stimulation* in 300um and 400um thick slices (*thickness*) across electrodes of discrete *distances* showed highly significant effects of *stimulation* ($F(1,426) = 171.44$, $p < 0.0001$) and significant interactions between *stimulation* and *distance* ($F(4,426) = 42.66$, $p<0.0001$). The slice *thickness*, compare colored lines in Figure 2.3e and 2.3f, also had a highly significant effect on measured coherence ($F(1,426) = 45.94$, $p<0.0001$) as did the interaction between *thickness* and *distance* ($F(4,426) = 7.72$, $p<0.0001$). The interaction between *stimulation* and slice *thickness* as well as the interaction between all three variables were not significant indicating that the slice thickness does not alter the effect of gamma oscillation induction nor does it change the fundamental relationship between stimulation and distance.

In the 300um thick slices, post hoc testing (simple main effects) indicated significant effects of carbachol stimulation on coherence between electrodes at 200 ($F(1,30) = 87.75$, $p<0.0001$) and 280um ($F(1,28) = 21.25$, $p<0.0001$) distances (Figure 2.3e). Similar analysis of the coherence calculations from the 400um thick slices also showed highly significant effects on coherence at 200 ($F(1,46) = 162.75$, $p < 0.0001$),

280 ($F(1,46) = 65.00$, $p<0.0001$), 400 ($F(1,44) = 4.13$, $p<0.05$) and 450um ($F(1,86) = 4.88$, $p<0.05$) distances (Figure 2.3f).

Increasing the density of connectedness across the bulb slice produced close to a 50% increase in the coherence magnitude in the 400 um thick slice with an average 200 um coherence value of 0.47 ± 0.032 (mean ± s.e.m) compared to 0.313 ± 0.048 in the 300 um thick slices. At 280 um, there was a 73% increase in the 400um thick slices (0.281 ± 0.031) compared to 0.162 ± 0.035. Furthermore, only the 400um thick slices showed a significant increase in coherence at 400 and 450um following carbachol application. These data support the hypothesis that the geometry of connectedness has a critical role in the synchronization of distant neural assemblies [20].

GABA(A) receptor blockade eliminated coherence across gamma oscillations.

The observed increase in measured coherence across the EPL in thicker slices, allowed us to more systematically explore the role GABAergic feedback in the EPL has on the coherence of OB gamma oscillations (Chapter 1). We predict that bath application of a GABA(A) receptor antagonist would fail to block gamma band oscillations, but these oscillations will show a reduction of recorded coherence across multiple electrodes.

We tested the hypothesis that coherent gamma band oscillations (20-55 Hz in our hands) are spatially synchronized by GABAergic activity in the bulb by blocking GABA(A) receptor activity through bath application of the GABA(A) receptor antagonist bicuculline methiodide (BMI). OB slices (400um thick) were placed in the recording well where 200uM BMI was applied to the bath and superfused over the

slice for minutes before application of 100uL of 186uM carbachol. Despite GABAergic blockade, carbachol induced gamma band oscillations in the OB slice as illustrated by the normalized FFT data (Figure 2.4a; averaged across 3 slices/ 17 electrodes; same method as Figure 2.2b). The average frequency of the peak power traces was 29.5 ± 1.07 Hz (n=17) with the distribution of peak power averages illustrated in Figure 2.4b. Note this shift in frequency to the lower gamma range compared to the carbachol application in aCSF (Figure 2.2c). Carbachol application in the presence of BMI did produce a significant increase in gamma band power compared to prestimulation integrated gamma power (paired t-test; $t(16) = 2.4$; $p<0.05$).

Carbachol application to 400um thick OB slices in the presence of 200uM BMI did produce recordable oscillations across multiple electrodes (n = 3 slices/ 6 reference electrodes). We calculated coherence across the multiple site oscillations. To distinguish true coherence from baseline levels of spurious coherence as a result of an overall increase in activity following GABAergic blockade, we estimated the latter by scrambling the pairings of reference electrodes with their corresponding peak frequencies and calculating the average pairwise coherence from these scrambled data (seen in Figure 1.4c, *dashed lines*). Simple main effects post hoc tests following two-factor ANOVA comparing unscrambled to scrambled data indicated that under control conditions (carbachol in aCSF), there was substantial true coherence among electrodes at 200 ($F(1,46) = 90.33$, $p<0.0001$) and 280 um ($F(1,46) = 30.33$, $p<0.0001$) distances.

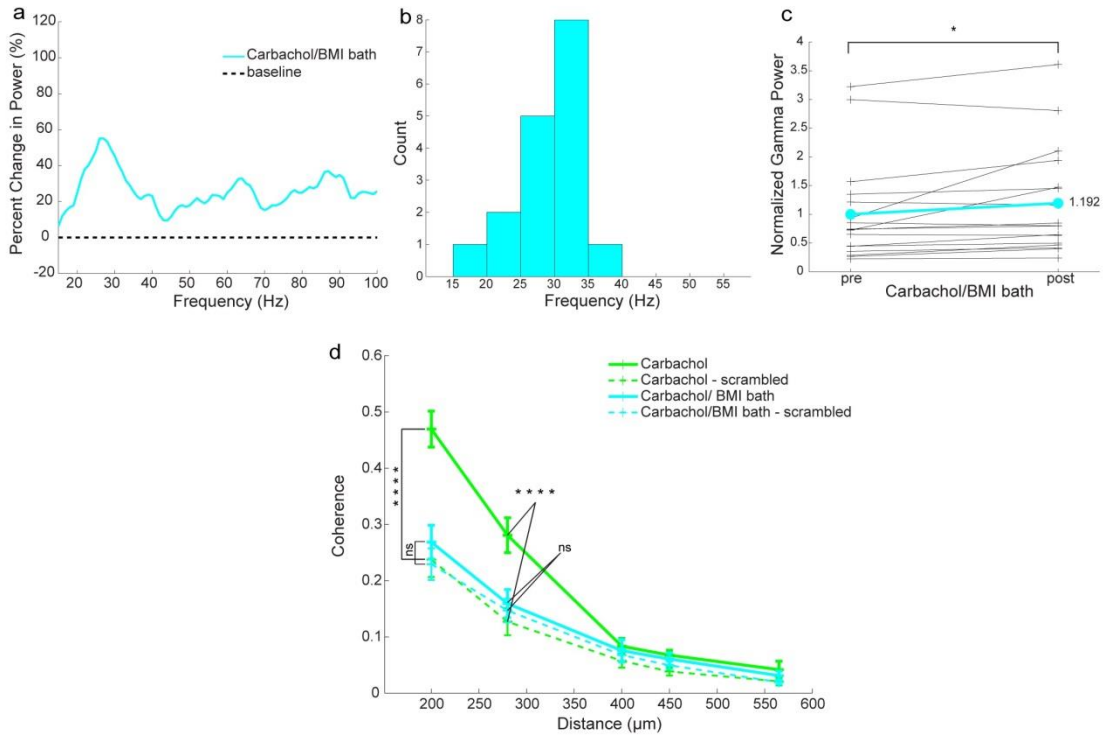

Figure 2.4. GABAergic blockade reduces coherence across oscillating bulbar regions. **(a)** Overlaid average power spectra following carbachol application to 400 um thick OB slice with 200uM BMI bath (n = 4 slices/17 electrodes) with emergent power normalized to baseline spectral power. **(b)** Histogram showing the cumulative average frequency of the peak power from each 80s traced oscillation induced by carbachol with BMI bath (n = 17). **(c)** Paired t-tests of the integrated gamma band (20-55Hz) of the convergent freqency data show the carbachol induced a significant increase in gamme band power despite the presence of BMI ($t(16) = 2.40$; $p < 0.05$) compared to baseline integrated gamma power. **(d)** Comparison of oscillation coherence across space from acetylchoine agonist induced oscillations in aCSF (solid line, *green*, same as Figure 2.3f) and during bath application of the GABA(A) receptor antagonist BMI (n = 3 slices/6 electrodes; 200 uM; solid line, *cyan*). To test for spurious coherence, the reference frequencies were scrambled between pairings of reference electrodes and their corresponding peak frequencies for both the aCSF and BMI data sets (broken lines; *green* and *cyan* respectively. Scrambling the reference frequencies significantly reduced the coherence across electrodes in aCSF (compare solid and broken *green* lines; Simple main effects post hoc tests; 200 and 280 um; $p < 0.0001$ in both cases), whereas the reduced coherence in the BMI bath was not significant (compare solid and broken *cyan* lines; $p > 0.11$ in all cases).

When GABA(A) receptors were blocked with BMI, there was no significant true coherence between electrodes at any distance ($p > 0.11$ in all cases).

Discussion

Our results show that the coherence power of gamma oscillations across olfactory bulb slices is modulated by slice thickness likely attributable to the density of lateral connectivity within the EPL. In the present experiments, we manipulated the long range connections by increasing the thickness of the slice and by decreasing GABAergic synaptic interactions. Blocking GABAergic transmission reduced the frequency of gamma oscillations and eliminated coherence across the OB slices.

Gamma oscillations induced by carbachol in 300um thick slices were similarly coherent (200um - 0.313 ± 0.05; 280um – 0.172 ± .04) compared to the oscillations induced by optical stimulation of ChR2 expressed in olfactory sensory neuron terminals (200um - 0.319 ± 0.13; 280um – 0.189 ± 0.06) and mGluR agonist induced gamma (200um - 0.333 ± 0.02; 280um – 0.187 ± 0.02). Increasing the slice thickness to 400um, though, increased the coherence magnitude of gamma oscillations beyond that of any other stimulation group (200um - 0.47 ± 0.03; 280um – 0.281 ± 0.03). These results support the hypothesis that the degree of underlying connectedness is critical in the production of spatially coherent gamma oscillations [20].

Consistent with our previous results, GABAergic blockade failed to block persistent gamma oscillations in OB slices (Chapter 1). Carbachol produced gamma band activity despite GABAergic blockade and these oscillations showed a reduction in frequency into the lower gamma band range (29.0 ± 1.05 Hz) that is similar to the

GABA(A) resistant oscillations induced by the application of mGluR agonists (29.0 ± 1.19 Hz) (Chapter 1). As proposed by the hybrid coupled oscillator hypothesis, we predicted that coherence between oscillating regions of the bulb is dictated by the degree of connectedness via GABAergic feedback across the EPL. Carbachol application to the 400um thick OB slices following GABAergic blockade produced gamma oscillations with coherence measurements (200um – 0.27 ± 0.03; 280um – 0.16 ± 0.03) similar to those produced by mGluR agonists in the presence of GABAergic blockade in 300um thick slices (200um – 0.27 ± 0.03; 280um – 0.13 ± 0.02) as seen in Figure 1.4c. Consistent with previous results, GABAergic blockade eliminated gamma oscillation coherence across oscillating regions of the OB slice. The pharmacological reduction of EPL connectedness provides strong evidence that coherent gamma oscillations recorded *in vivo* require extensive GABAergic feedback across the OB.

These data further support the hybrid-coupled oscillator hypothesis (Chapter 1) that GABAergic feedback from GCs is important for synchronizing glomerular oscillators but not for local glomerular synchronization. These results contrast the current inhibition based theories of gamma band rhythmogenesis in the hippocampus and cortex. Gamma oscillation frequency in the hippocampus has been shown to be sensitive to the decay constant of GABA(A) receptors. Increasing the GABA(A) decay constant through application of pentobarbital effectively reduced the oscillation frequency leading to the interpretation that hippocampal oscillation frequency is determined by GABAergic activity specifically through a network of mutual inhibition [21]. Likewise, gamma band oscillations in the barrel cortex can be induced by optically

stimulating ChR2 expression in fast spiking inhibitory cells [22]. Our results suggest that inhibition primarily functions to synchronize spatially segregated glomerular columns. This feedback inhibition could constrain MC timing by phasic reset of the STOs leading to an increased network frequency and globally coherent gamma activity across the bulb.

REFERENCES

1. Murthy, V. N. & Fetz, E. E. Synchronization of neurons during local field potential oscillations in sensorimotor cortex of awake monkeys. *J. Neurophysiol.* **76,** 3968–3982 (1996).

2. Gray, C. M., König, P., Engel, A. K. & Singer, W. Oscillatory responses in cat visual cortex exhibit inter-columnar synchronization which reflects global stimulus properties. *Nature* **338,** 334–337 (1989).

3. Bieri, K. W., Bobbitt, K. N. & Colgin, L. L. Slow and Fast Gamma Rhythms Coordinate Different Spatial Coding Modes in Hippocampal Place Cells. *Neuron* **82,** 670–681 (2014).

4. Eeckman, F. H. & Freeman, W. J. Correlations between unit firing and EEG in the rat olfactory system. *Brain Res.* **528,** 238–244 (1990).

5. Kay, L. M. & Freeman, W. J. Bidirectional processing in the olfactory-limbic axis during olfactory behavior. *Behav. Neurosci.* **112,** 541–553 (1998).

6. Beshel, J., Kopell, N. & Kay, L. M. Olfactory bulb gamma oscillations are enhanced with task demands. *J. Neurosci. Off. J. Soc. Neurosci.* **27,** 8358–8365 (2007).

7. Stopfer, M., Bhagavan, S., Smith, B. H. & Laurent, G. Impaired odour discrimination on desynchronization of odour-encoding neural assemblies. *Nature* **390,** 70–74 (1997).

8. MacLeod, K., Bäcker, A. & Laurent, G. Who reads temporal information contained across synchronized and oscillatory spike trains? *Nature* **395,** 693–698 (1998).

9. Friedman, D. & Strowbridge, B. W. Both electrical and chemical synapses mediate fast network oscillations in the olfactory bulb. *J. Neurophysiol.* **89,** 2601–2610 (2003).

10. Neville, K. R. & Haberly, L. B. Beta and gamma oscillations in the olfactory system of the urethane-anesthetized rat. *J. Neurophysiol.* **90,** 3921–3930 (2003).

11. Martin, C., Gervais, R., Chabaud, P., Messaoudi, B. & Ravel, N. Learning-induced modulation of oscillatory activities in the mammalian olfactory system: the role of the centrifugal fibres. *J. Physiol. Paris* **98,** 467–478 (2004).

12. Lagier, S., Carleton, A. & Lledo, P.-M. Interplay between local GABAergic interneurons and relay neurons generates gamma oscillations in the rat olfactory bulb. *J. Neurosci.* **24,** 4382–4392 (2004).

13. Lepousez, G. & Lledo, P.-M. Odor Discrimination Requires Proper Olfactory Fast Oscillations in Awake Mice. *Neuron* 1–15 (2013). doi:10.1016/j.neuron.2013.07.025

14. Brea, J. N., Kay, L. M. & Kopell, N. J. Biophysical model for gamma rhythms in the olfactory bulb via subthreshold oscillations. *Proc. Natl. Acad. Sci. U. S. A.* **106,** 21954–21959 (2009).

15. Desmaisons, D., Vincent, J. D. & Lledo, P. M. Control of action potential timing by intrinsic subthreshold oscillations in olfactory bulb output neurons. *J. Neurosci. Off. J. Soc. Neurosci.* **19,** 10727–10737 (1999).

16. Rubin, D. B. & Cleland, T. A. Dynamical mechanisms of odor processing in olfactory bulb mitral cells. *J. Neurophysiol.* **96,** 555–568 (2006).

17. Ermentrout, G. B. & Kopell, N. Fine structure of neural spiking and synchronization in the presence of conduction delays. *Proc. Natl. Acad. Sci. U. S. A.* **95,** 1259–1264 (1998).

18. Fisahn, A., Pike, F. G., Buhl, E. H. & Paulsen, O. Cholinergic induction of network oscillations at 40 Hz in the hippocampus in vitro. *Nature* **394,** 186–189 (1998).

19. Fellous, J. M. & Sejnowski, T. J. Cholinergic induction of oscillations in the hippocampal slice in the slow (0.5-2 Hz), theta (5-12 Hz), and gamma (35-70 Hz) bands. *Hippocampus* **10,** 187–197 (2000).

20. Bazhenov, M., Rulkov, N. F. & Timofeev, I. Effect of synaptic connectivity on long-range synchronization of fast cortical oscillations. *J. Neurophysiol.* **100,** 1562–1575 (2008).

21. Whittington, M. A., Traub, R. D. & Jefferys, J. G. Synchronized oscillations in interneuron networks driven by metabotropic glutamate receptor activation. *Nature* **373,** 612–615 (1995).

22. Cardin, J. A. *et al.* Driving fast-spiking cells induces gamma rhythm and controls sensory responses. *Nature* **459,** 663–667 (2009).

CHAPTER 3

A 768-CHANNEL CMOS MICROELECTRODE ARRAY WITH ANGLE SENSITIVE PIXELS FOR NEURONAL RECORDING

Ben Johnson[1], Shane T. Peace[2], Albert Wang[1], Thomas A. Cleland[3], and Alyosha Molnar[1]

[1]Dept. Electrical and Computer Engineering

[2]Dept. Neurobiology & Behavior

[3]Dept. Psychology

Cornell University

Ithaca, NY 14853

Introduction

How networks of neurons work together to perform complex tasks and propagate information is an active area of research. To effectively study neural ensembles, neurophysiologists employ microelectrode arrays (MEA) to simultaneously acquire electric field activity across relatively large areas of tissue. The advantages of increasing the number of recording electrodes include: 1) the possibility for a greater number of single cell recordings and 2) spatially broad analysis of local field potentials (LFPs) that can provide insights into how and why neuronal ensembles synchronize their activity. MEA data are an invaluable resources for computational neuroscience and for the study of biological learning, acute and chronic drug effects, and physiological disorders.

Conventional planar MEAs are noninvasive and function by recording electrical extracellular activity with metal electrodes (Figure 3.1). Signals detected at the electrode interface are amplified, passed through a low-pass filter, and then digitized. MEAs are well suited for extended in vitro studies using either tissue preparations, such as retinas or brain slices[1], or neuronal cell cultures[2]. Most commercially available MEAs are fabricated on passive, patterned substrates which use off-substrate amplifiers. While these MEAs typically have between 60-256 electrodes, passive routing limits the electrode scalability. CMOS MEAs can achieve a higher spatial resolution and a large effective recording area by multiplexing channels onto fewer wires. Furthermore, they can include additional modalities, such as optical recording[1], electrical stimulation[2], or temperature sensors[3].

Another effective way to study neural networks with MEAs is in conjunction with optical stimulation. In visual neuroscience, computer-generated patterns of light can be used to stimulate retinal photoreceptors while electrically recording activity from the ganglion cells, the retinal output. Likewise, optogenetics allows researchers to create light-sensitive cells in other biological systems to understand the way they process information. For example, neuronal cells expressing the light- reactive protein channelrhodopsin-2 can be excited optically, circumventing the need for either

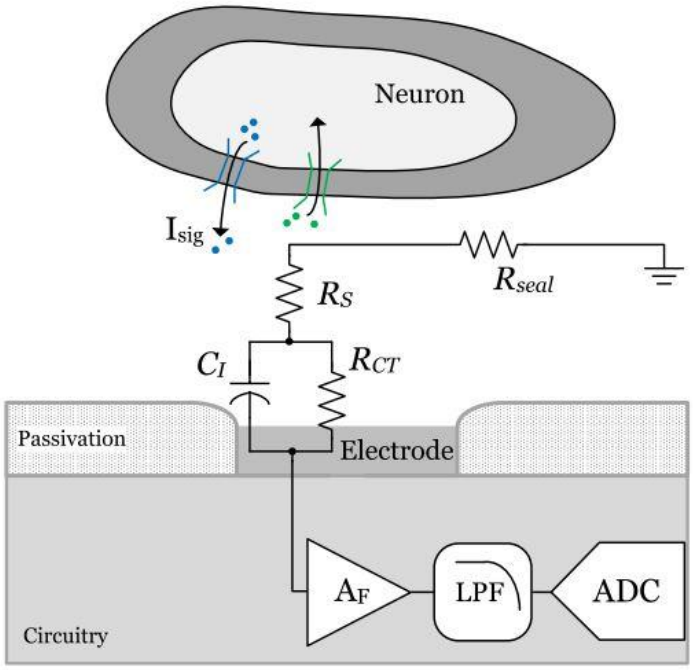

Figure 3.1. Concept of planar MEA recording

electrical stimulation which creates large recording artifacts, or chemical stimulation which is nonspecific[4]. Optical stimulation can be spatially and temporally precise, cell-specific, and contact-free. Therefore, optical stimulation allows researchers to control the inputs of a neural system while an MEA allows them to record multiple intermediate and output nodes of the network.

Passive MEAs are often built on transparent substrates allowing for visual correlation of electrode location, tissue and stimulus. Active MEAs on silicon substrates are opaque and severely limit this capability. Furthermore, CMOS MEAs can still suffer from some of the same scalability limitations of passive MEAs. State-of-the-art CMOS arrays typically tradeoff between electrode density, noise performance, and sampling rate. Therefore, the aim of this work is provide researchers with an MEA that overcomes the limitations of both traditional passive and active MEAs for slice research. The presented MEA has a high spatial resolution, a large recording area, and integrated angle-sensitive pixels (ASP[5]) to correlate optical stimuli with recorded activity. Additionally, the sensor array requires little post-CMOS processing for biocompatibility and can record from all sensors simultaneously.

This paper is organized as follows. Section II discusses the characteristics of MEA recordings as motivation for the design of the CMOS array and other state-of-the-art CMOS arrays. Section III details the system design and packaging of the sensor array. Section IV presents test results of the fabricated array and neural data acquired from a mouse olfactory bulb slice.

Neural signals from MEA recordings

Methods

The design was dictated by the characteristics of extracellular biopotentials recorded from olfactory bulb slices. A commercially available MEA (MEA60-Up-System, MCS GmbH) with 60 TiN electrodes was used to record extracellular fields. The electrodes had a diameter of 30μm and a pitch of 200μm. Slices were horizontally taken with a vibrating microtome with a nominal thickness of 300μm. During

recording, slices were perfused with artificial cerebrospinal fluid (aCSF) containing (in mM) 125 NaCl, 25 NaHCO3, 1.25 NaH2PO4, 25 glucose, 3 KCl, 1 MgCl2. The solution was heated to 34 degrees Celsius using an inline heater and oxygenated with carbogen (95% O2, 5% CO2). Slices were held down by a chrome harp with nylon netting.

Extracellular Biopotentials

According to the literature, discernible extracellular biopotentials typically range in amplitude from 10μV to about 5mV, with power in the 10-200Hz band for LFPs and 200Hz-5kHz band for action potentials[6]. Figure 3.2 shows the measured power spectrum of endogenous slice activity with several electrodes (n = 13). The measured spectrum was calculated by 1) averaging power spectra from a 50s long single electrode recording with 1s epochs, then 2) averaging that power spectrum with n other electrodes. The power spectrum reflects contributions from both LFP and action potentials. The LFP power peaks around 45Hz, which corresponds to the gamma band in slice (30-70Hz[7]). Gamma oscillations are ubiquitous in the brain and are indicators of synchronous cellular activity. While gamma oscillations can occur endogenously, they can also be induced chemically with glutamate receptor agonists. A spectrogram of an induced gamma oscillation is shown in Figure 3.3. Oscillations were also induced by optical stimulation of slices from transgenic mice expressing channelrhodopsin-2 in the olfactory sensory neuron axons. To utilize the temporal and spatial precision of optical stimuli, the proposed MEA uses photopixels to correlate light stimuli with recorded electrical activity. Neural acquisition systems for in vivo recording deal with large voltage offsets from LFP, and often separate the LFP and spike bands to alleviate the dynamic range requirement of the ADC[8]. However, in this experiment the largest recorded biopotentials were on the order of 200μVpp. Furthermore, the frequency content of LFP and spiking can overlap. The resultant spectral contamination means that traditional low- pass filtering methods to remove spike contributions from the LFP band may give rise to unwanted spurious correlations, problematic when studying the causal relationship between LFP

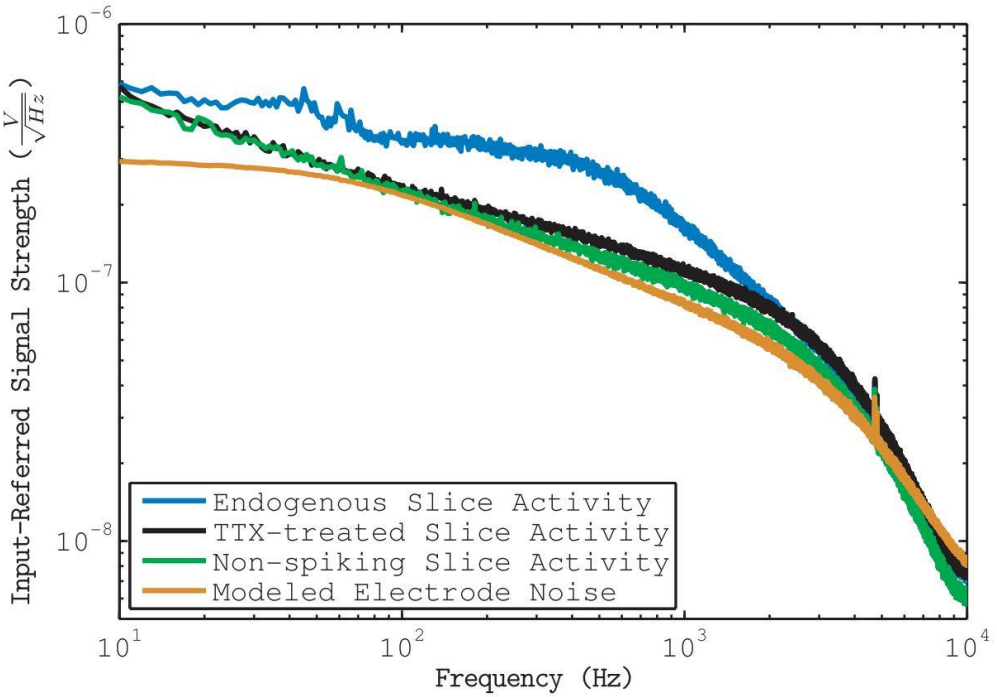

Figure 3.2. Power spectra from MEA slice recordings.

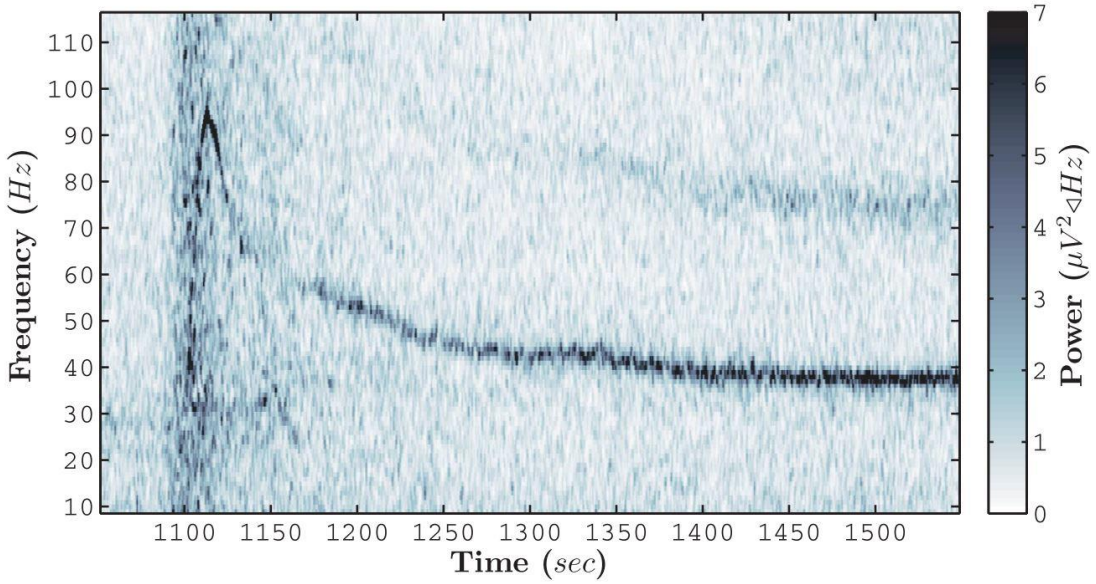

Figure 3.3. A spectrogram of an induced gamma oscillation

and spiking. Spike removal algorithms have been shown to effectively remove spike contributions from the LFP band, assuming the recorded signal is wideband[9,10]. Thus, the proposed MEA does not separate the LFP and spike bands on chip since more sophisticated filtering is required.

Background Noise Level

Recording neural signals requires low-noise instrumentation. To understand the background noise level associated with recording from slice, a sodium channel blocker, tetrodotoxin (TTX), was applied during the recordings (n = 13). This yields an estimate of the recording noise level because the spiking and oscillations have been blocked. An additional background level was obtained by averaging spectra recorded from electrodes covered by slice tissue without discernible spikes or oscillations (n = 9). The total integrated noises were 7.2μVrms and 6.5μVrms, respectively. With microelectrodes, the dominant noise source in extracellular recording typically arises from the electrode-electrolyte interface, not the recording circuitry which is often well controlled[11]. Using methods presented in[12] and[13] for the circuit model in Figure 3.1, we estimated the charge transfer resistance (R_{CT}) of the interface to be 4.7MΩ, the parallel interface capacitance (C_I) to be 495pF, and the spreading resistance (R_S) to be 12kΩ. Neglecting the Warburg impedance, the estimated noise from the interface was 4.9μVrms. The recording circuitry had little effect on the overall noise level (2.6μVrms), which was measured by shorting the input of the recording amplifier to ground (n = 3). In terms of frontend amplifier design, circuit noise levels much below 2.4μV contribute little to the overall noise level and are likely overdesigned, consuming unnecessary power or area. Circuit noise above 5.3μVrms, however, is likely to be the dominant noise source for electrodes with similar geometry.

Spatial Spread

Measured persistent epochs (> 5 min) of gamma oscillations (30-70Hz) spanned over 600μm laterally while spiking activity from individual cells typically spread less than 100μm. This is comparable to measurements from hippocampal

slices[14] and modeled results for synchronous network activity[15]. The spatial reach of gamma oscillations was determined by finding the coherence between the electrode with the highest gamma power and all other electrodes, where the coherence magnitude between two electrode recordings in the frequency domain is given by:

$$C_{xy}(f) = \frac{| < P_{xy}(f) >_n |}{\sqrt{< P_{xx}(f) >_n \cdot < P_{yy}(f) >_n}},$$

Pxx and Pyy are autocorrelations and Pxy represents the cross-correlation between the two electrodes. Note that coherence for every 1Hz frequency bin was calculated over n epochs of 1s, where n = 150. Figure 3.4 shows an example spatial coherence profile. In theory, adjacent electrodes exhibit no coherence in the absence of synchronous activity ($\mu 0 = 0$) while oscillatory activity spanning multiple electrodes will be highly correlated. The variance of coherence was calculated using 58 electrodes and 20 frequency bins (21-40Hz) for a total of 1160 measures of coherence. Based on the spatial expanse of LFP, a useful planar MEA should have an active area larger than 1mm on a side to accommodate large synchronous oscillations from an entire slice and have an electrode pitch of less than 100μm to fully sample extracellular action potentials.

Design Requirements

Table 3.1 provides a summary of the design requirements for the CMOS sensor array derived from experimental MEA recordings. While previous work has achieved subcellular electrode pitch (<10μm) and low-noise amplification (2.4μVrms), the array record from a static selection of 126 electrodes simultaneously[2]. In principle, these sites can be multiplexed faster than the bandwidth of the neural signals, allowing multiple sites to be measured each sample cycle. The difficulty with high-speed multiplexing before amplification is that noise from the interface is not filtered and is therefore aliased into relevant signal bands. Other work has used electrode-level amplification to increase the number of recording channels. Berdondini et al.[16], provide pixel-level amplification with 4,096 small pitch electrodes (42μm) but

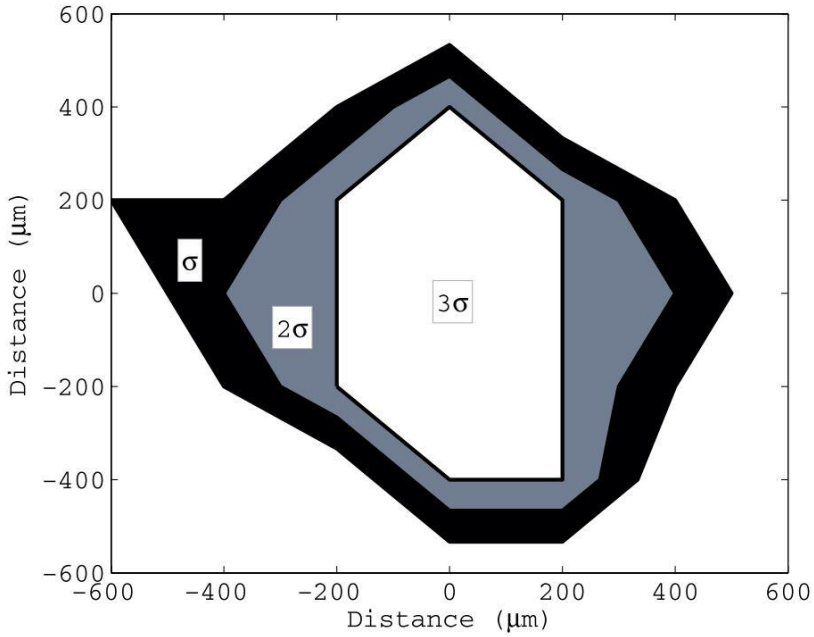

Figure 3.4. Spatial coherence profile of a 33 Hz olfactory bulb slice gamma oscillation (μ0 = 0, sigma = 0.067). The origin represents the location of the electrode with the highest power in the gamma band.

TABLE 3.1

DESIGN REQUIREMENTS OF THE CMOS SENSOR ARRAY

Specification	
Signal Bandwidth	10Hz - 3kHz
Sampling Rate	10kHz
Circuit Noise	$2.4\mu V_{rms}$ - $5.3\mu V_{rms}$
Dynamic Range	>30dB
Electrode Pitch	$<100\mu m$
Spatial Extent	$>600\mu m$

sacrifices noise performance (11μVrms). Another high-density array[17] has an even finer sensor pitch (7.8μm) and more sensors (16,384), but with a much higher noise level (70μVrms). Therefore the primary design challenge of CMOS MEAs is designing a low- noise amplifier with a very small area and with a scalable data read-out.

SYSTEM DESIGN

System Description

The hybrid sensor array consists of 768 metal electrodes with local amplification and digitization and 2,048 photopixels. The MEA was fabricated in a standard 130nm CMOS process with an active area of 1.6mm by 1.6mm (Figure 3.5). An input clock (F_{in} = 40MHz) feeds a 12-bit counter in the digital core which then generates the control signals and clocks for the rest of the chip. Each sensor site is sampled at a rate of 10kHz as determined by the MSB of the counter, which is the main clock rate divided by 2^{12}. Figure 3.6 shows the timing diagram of the array. Sensor sampling is interleaved so that data can be output continuously at a rate equal to the main clock. There are four data output channels, each of which is fed by its own 640-bit shift register. Half of the sensors are sampled simultaneously while the other half of the sensors load and then shift data off the chip. A global 20kHz ramp signal is used as an ADC reference voltage at every sensor. The ramp is generated by a PFET current DAC controlled by the counter with a resistive load to translate the output current into a voltage. Since control signals are generated globally and the outputs are digitized, the design is highly scalable. The limiting factor of this design was the available die area.

Four-Sensor Subunit

Figure 3.7 shows the four-sensor subunit. Each subunit is comprised of three recording electrodes (A, B, C) and a set of 8 ASPs (D). Each site is allocated an area

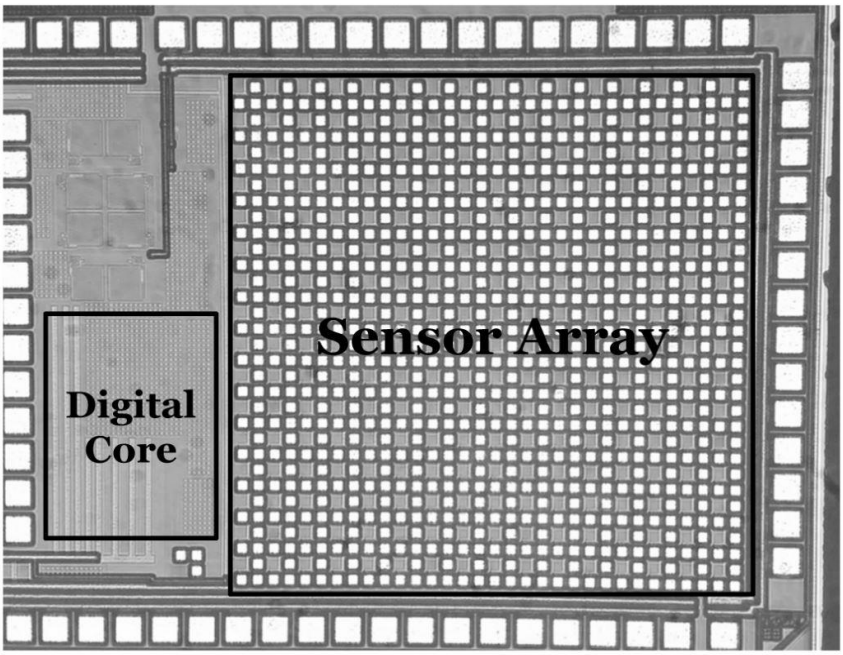

Figure 3.5. Die photograph of the sensor array.

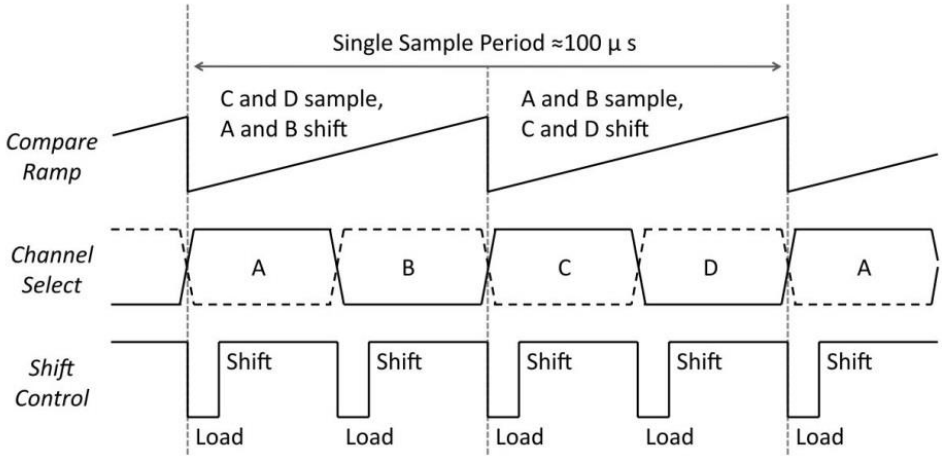

Figure 3.6. Timing diagram of control signals. Half of the sensors are sapled concurrently while the other half shifts data to the output. *Channel Select* controls the subset of sensors that are shifting data and *Shift Control* facilitates the loading and shifting of the global shift registers.

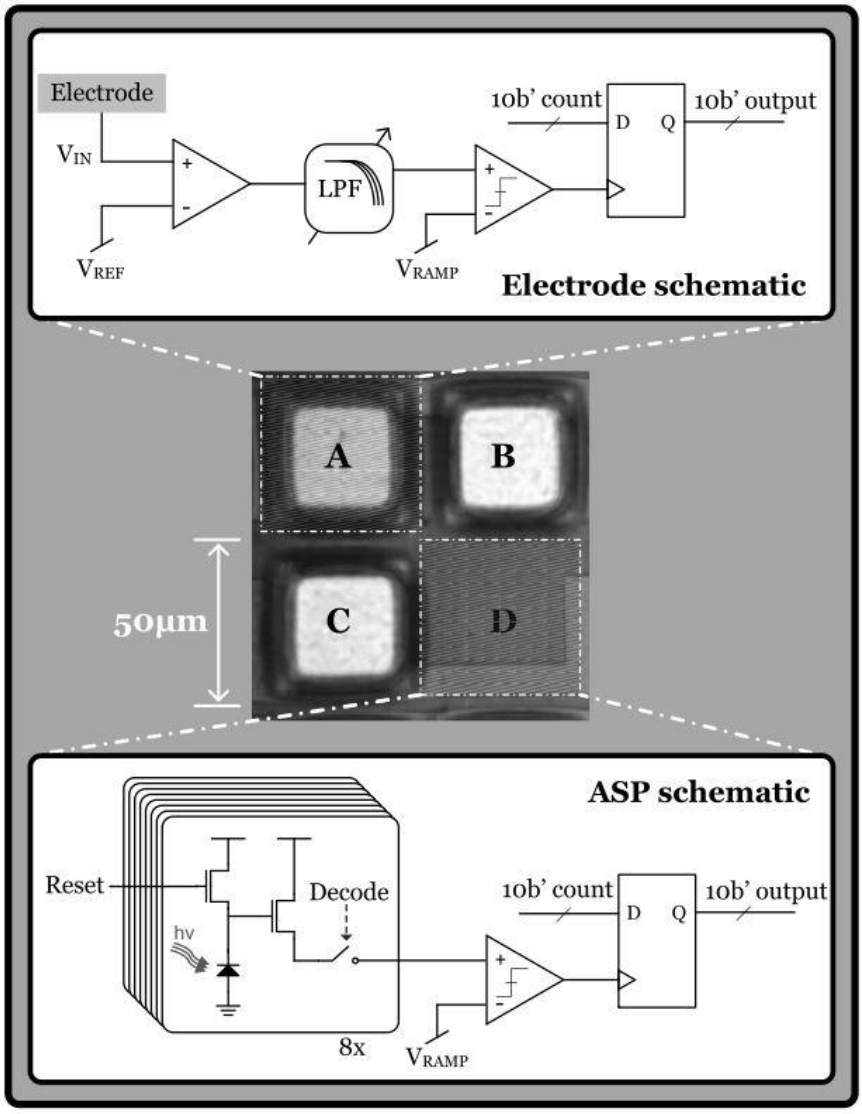

Figure 3.7. Photo and architecture of four-sensor subunit. Each subunit is comprised of 3 recording electrodes (**A, B, C**) and a set of 8 ASPs (**D**).

of 50μm by 45μm with an additional 50μm by 5μm of each sensor site used as part of the global shift register, which streams out the locally stored data.

The backend for the recording electrodes and the ASPs are identical. The comparator digitizes the analog signal from the sensor by comparing it to the global ramp signal. Each step of the ramp corresponds to a 10-bit value generated by the counter in the digital core. When the ramp signal is larger than the amplified signal, the comparator clocks the latch, storing the 10-bit number locally, and then shuts down to conserve power and reduce switching noise until the next sampling cycle.

Electrode Circuitry Design

Each recording electrode site contains an amplifier, a switched-capacitor low-pass filter, a comparator, and a 10-bit latch as shown in Figure 3.7. The metal electrode interface is defined by a passivation opening over the top metal and is formed during the standard CMOS fabrication process. V_{REF} is the applied reference potential of the electrolyte bath and is common to all the amplifiers of the array. Figure 3.8 shows a schematic of the folded cascode front-end amplifier. Traditional neural amplifiers use large input transistors to reduce flicker noise and large capacitors (20pF) to block electrochemical offsets[6]. To reduce area in this design, the front-end amplifier uses chopping modulation to reduce the flicker noise of the amplifier and bias the input transistors. In simulation, the total input-referred noise voltage of the amplifier over a 10kHz bandwidth is reduced by a factor of 6.6 when chopping modulation is used. The size of the input transistors are small to maintain a high input impedance (>20MΩ at 1.25MHz). To achieve the same performance without chopping modulation, the input transistor area would need to be increased by a factor of 43.

Low-pass filtering is needed before sampling in order to prevent aliasing of high-frequency noise from the tissue, electrode-electrolyte interface, and the amplifier. Rather than using a large load capacitor to pull the amplifier output pole to below half the sampling frequency, a much smaller MOS capacitor (C1) was used to prevent aliasing of high-frequency chopping artifacts, followed by a switched-capacitor low-pass filter ($\omega L = f_{chop}C2/C3$). This significantly decreases the required area to get the

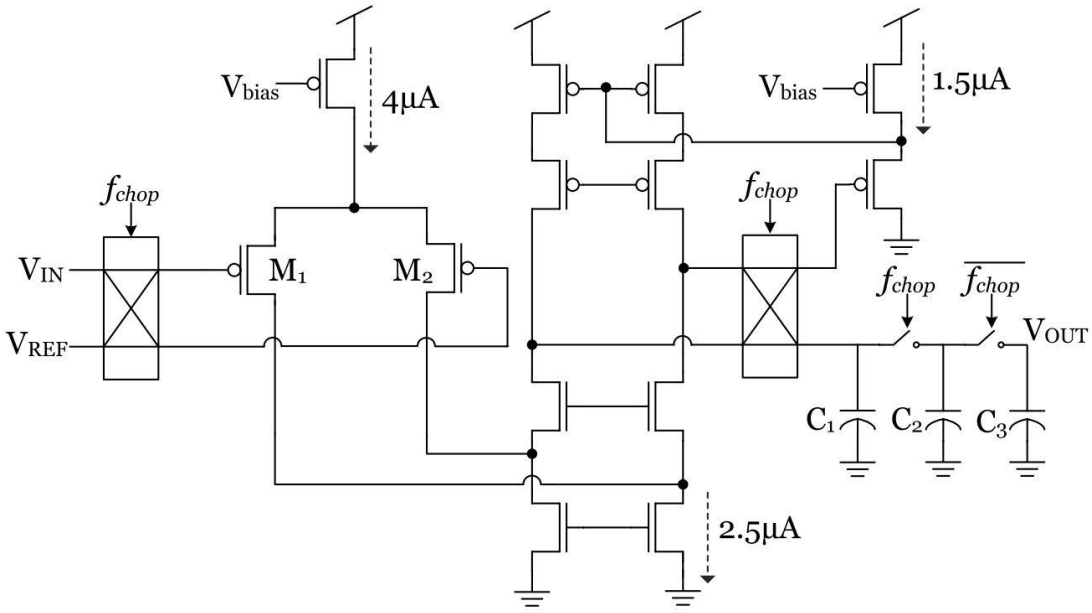

Figure 3.8. Schematic of the front-end amplifier with a switched-capacitor filter.

desired pole without lowering the amplifier current, which would increase thermal noise. Furthermore, the chopping frequency controls the low-pass frequency corner. Note that the chopping frequency is controlled directly by the main clock so that the comparator always samples with the same phase. Another advantage of switched-capacitor filters is that they are relatively process invariant since their corner is set by the switching frequency and a ratio of two nearby capacitors. The amplifier and low-pass filter occupy an area of 800μm2, about 25 times smaller than neural amplifiers in MEAs with similar performance[18].

.

Angle-Sensitive Pixel Design

In place of a front-end amplifier, one-quarter of the sensor sites (D from Figure 3.7) contain eight distinct ASPs. ASPs, first introduced in 2011[19], are devices which are sensitive to the angle of incident light and have been used to localize multiple fluorescent sources in 3D space[5] and perform postcapture computational refocus of visual scenes[20]. ASPs were implemented rather than standard photopixels because they can provide a more complete description of the light field. This is useful for understanding the scattering of stimulus light in tissue or localizing external electrodes with respect to the array. In general, ASPs use two CMOS metal gratings over a photodiode where the pitch and height between the gratings define the angular selectivity. The lower grating is used to block or pass the periodic intensity pattern generated by light striking the top grating as a function of its lateral offset. In this design, the ASPs employ two local, stacked diffraction gratings on CMOS metal layers 5 and 3 directly over a p-implant/n-well photodiode. At each sensor site there are two orientations of top diffraction grating (vertical and horizontal), and four types of bottom grating offset relative to the top grating ($\alpha = 0, \pi/2, \pi$, or $3\pi/2$) for a total of eight 22 ASP variants with α defining the angle of peak photodiode response. Since the sampling rate needed for an ASP is much lower than an electrode, only one of the eight ASP subtypes are digitized each time for an effective sampling rate of 1.25 kHz.

Packaging

A major difficulty with using CMOS sensors is ensuring biocompatibility and protecting wirebonds from the electrolyte solution. Most post-CMOS packaging techniques use lithographically defined epoxy or patterned PDMS to encapsulate wirebonds[21]. To simplify post-processing, epoxy was applied under a light microscope without a mask and used to encapsulate the wirebonds and define a well around the active area. The top metal of this process is aluminum, which corrodes easily in saline[22] and is also cytotoxic[23]. To prevent the electrodes from corroding, the electrodes were electroplated with platinum. Platinum is nontoxic and also decreases electrode impedance. Electroplating was performed by filling the well with a platinizing solution (chloroplatinic acid, lead acetate, hydrochloric acid). 1.5V was applied to a platinum counter-electrode to pull current through the electrodes.

EXPERIMENTAL RESULTS

System Characterization

Figure 3.9 shows the measured transfer function of the front-end amplifier with two different chopping frequencies. The amplifier consumed a total of 6μA from a 1.5V supply. The amplifier's bandwidth and midband gain changed from 3.6kHz and 43.5dB with a 1.25MHz chopping frequency to 2.3kHz and 43.9dB with a 700kHz chopping frequency. The total measured input-referred noise was 4.1μVrms over the 3.6kHz bandwidth, corresponding to a NEF of 6.5[24]. The ramp ADC achieved an ENOB of 8.7 bits with a 512mVpp ramp, which corresponds to a resolution of 7.9μV at the input (fs = 10kHz, fin = 100Hz). The total power consumption of the sensor core was about 13.3mW, with 55% of the power consumed by the frontend amplifiers.

Figure 3.10A shows the normalized response of four ASP subtypes to changes in incident angle. The light was generated by a 470nm LED which was kept at a fixed distance and rotated by a micromanipulator around the sensor array. Note that the output of an ASP is a function of both intensity and incident angle, which can result in ambiguity between a bright source at a blocked angle or a dim source at a passed angle. This ambiguity is resolved by taking the difference between complementary

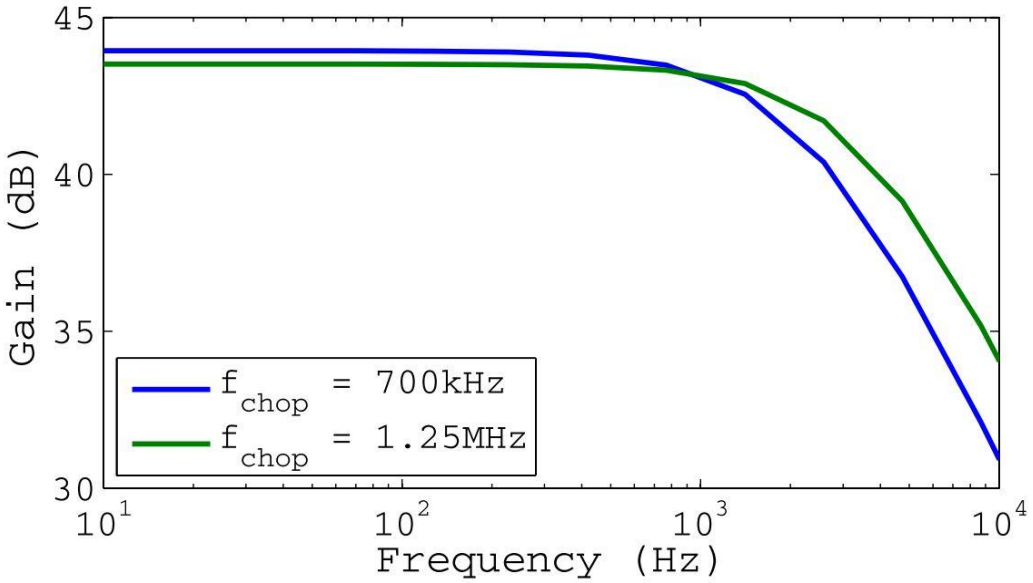

Figure 3.9. Measured transfer function of the front-end amplifier with two different chopping frequencies.

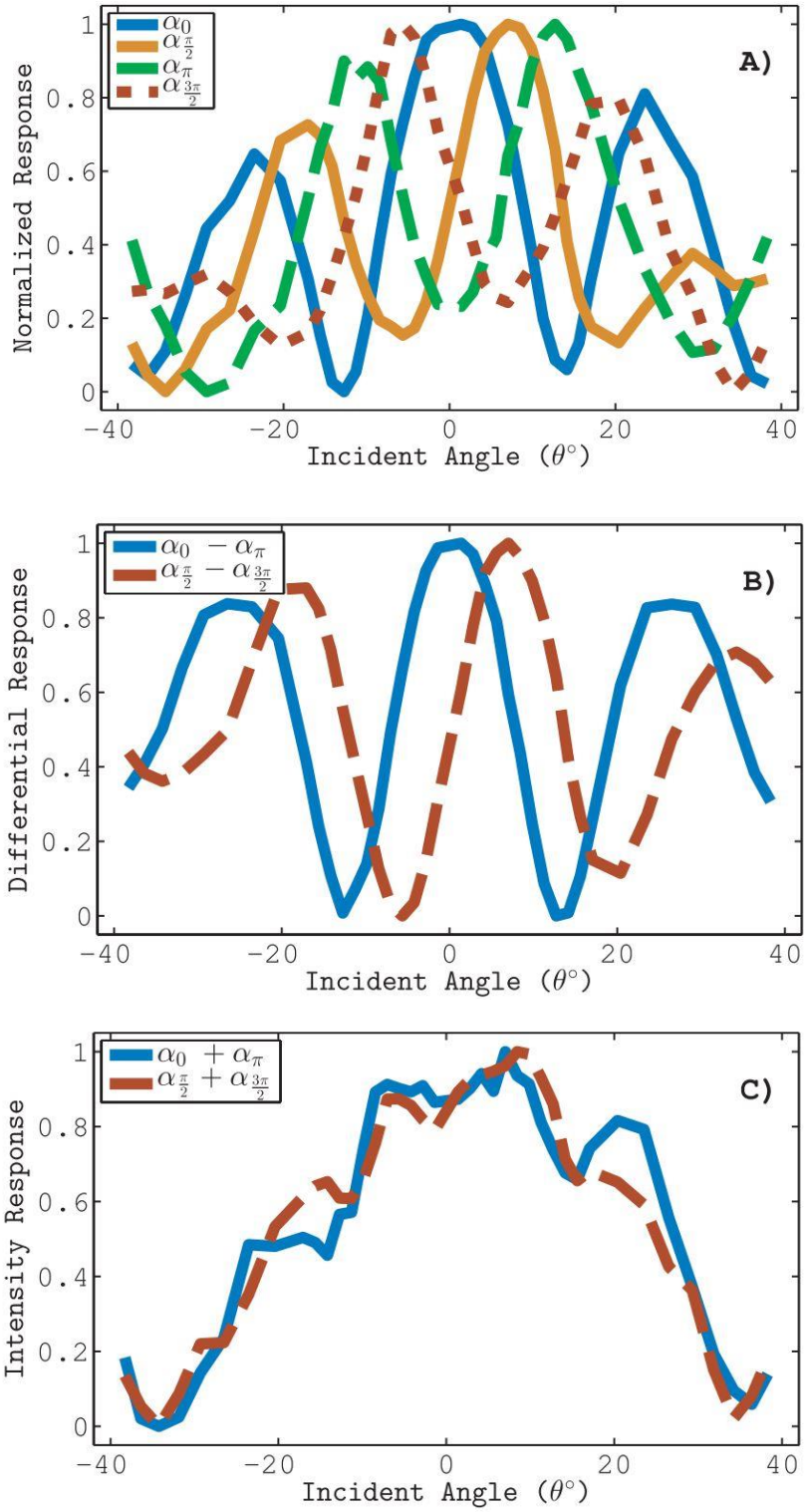

Figure 3.10. **A)** Normalized angular response of four ASP subtypes with different analyze grating offsets. **B)** The difference of complementary ASP subtypes and **C)** their sum.

ASPs, as shown in Figure 3.10B. The sum of the complementary ASPs encodes the intensity of the incident light (Figure 3.10C).

Measurement Results

Since each front-end amplifier operates open loop, there is a slight gain mismatch between electrodes. To calibrate and demonstrate array functionality, the well was filled with aCSF and stimulated with a 1mV sine wave through a silver chloride wire. Figure 3.11A shows a three-dimensional map of the input-referred rms voltage recorded by the array. The average gain across the array was 43dB with a standard deviation of 1.8dB. Figure 3.11B shows a 35ms overlay of three adjacent electrodes from the experiment in Figure 3.11A.

To demonstrate the functionality of the optical read-out, a 250μm diameter platinum reference electrode was fixed 200μm above the sensor array. First, an intensity image (sum of complementary ASP subtypes) was captured using an LED illumination source. Then, using synthetic refocus techniques[20], the image was computationally refocused in software as shown in Figure 3.12. Refocusing uses the information of the difference between complementary ASP subtypes and then convolves them with scaled, oriented Gabor filters.

To confirm that the sensors could provide sufficiently robust, low noise recording across the full range of biologically relevant signal bands, they were used to record both LFP and spiking activity. The tissue preparation was identical to that used in Section II. A power spectrum of oscillatory activity from a 300μm thick mouse olfactory bulb slice is shown in Figure 3.13. This data, unfiltered in software, shows an oscillatory peak at the gamma band and a sharp peak at 60Hz due to line noise. The line noise enters the system through the gravity-fed perfusion system and is not inherent to the circuitry. Gamma oscillations arise in the olfactory bulb and change in frequency over time, resulting in a broader peak than the constant frequency line noise. Endogenous spiking activity recorded from the slice is shown in Figure 3.14. These data were band-pass filtered in MATLAB ($200\text{Hz} \leq \text{fbp} \leq 6\text{kHz}$) to remove LFP activity.

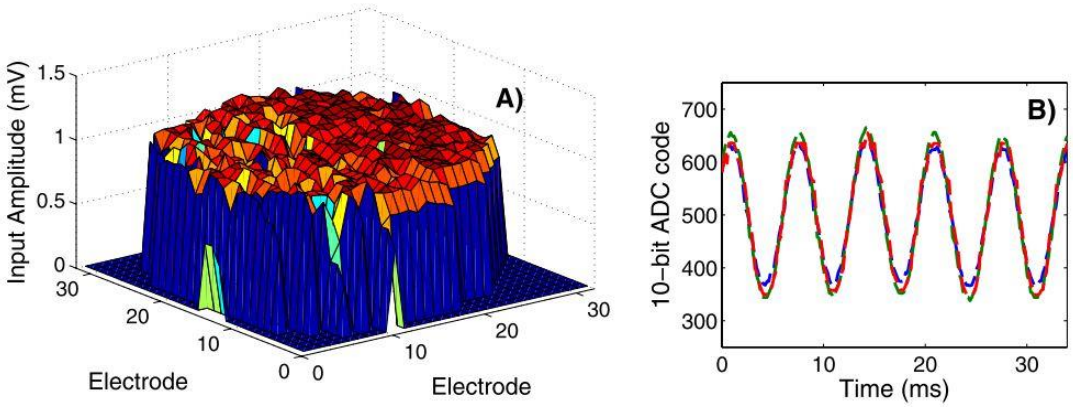

Figure 3.11. **A)** Array recording of 1mV sinusoid through a sliver chloride wire in aCSF with V_{REF} set to circuit ground. The voltage is the rms value of the input signal. **B)** Digitized output of the three adjacent electrodes of data shown in **A**.

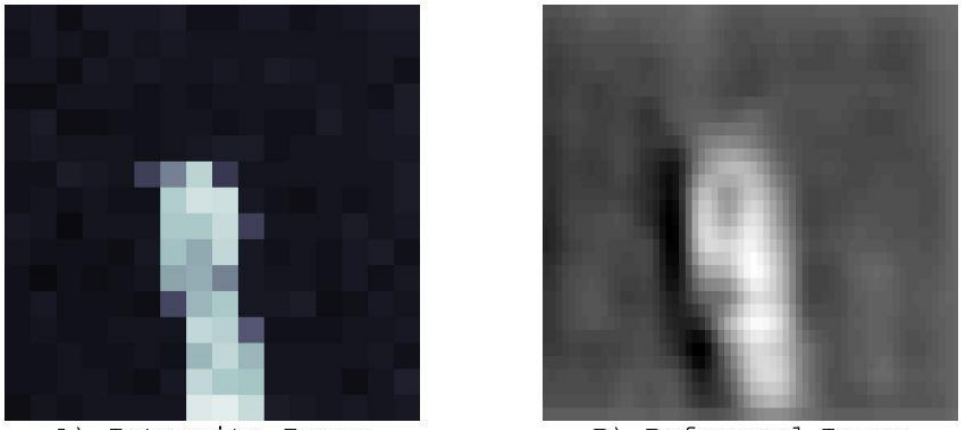

Figure 3.12. **A)** Lensless intensity image captured with ASPs of a platinum reference electrode over the sensor array and **B)** computationally refocused image.

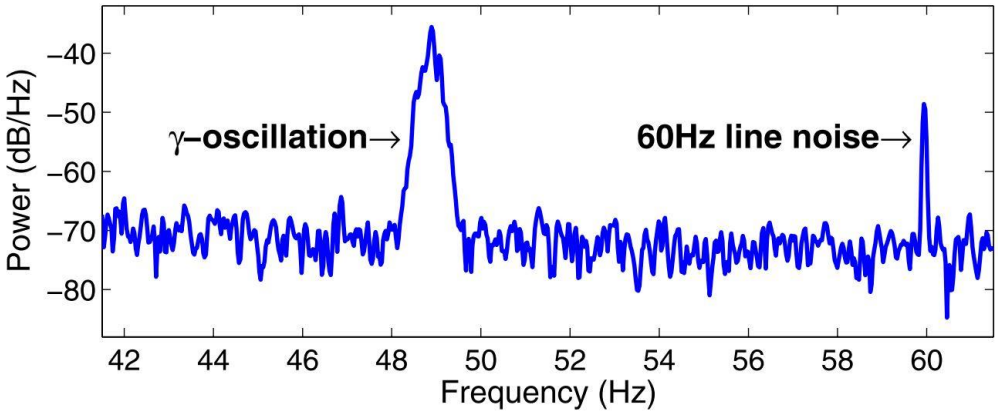

Figure 3.13. Power spectrum of a long-lasting gamma oscillation in the olfactory bulb. The gamma oscillation varies in frequency over time creating a broader peak while the 60Hz line noise remains constant resulting in a narrow peak.

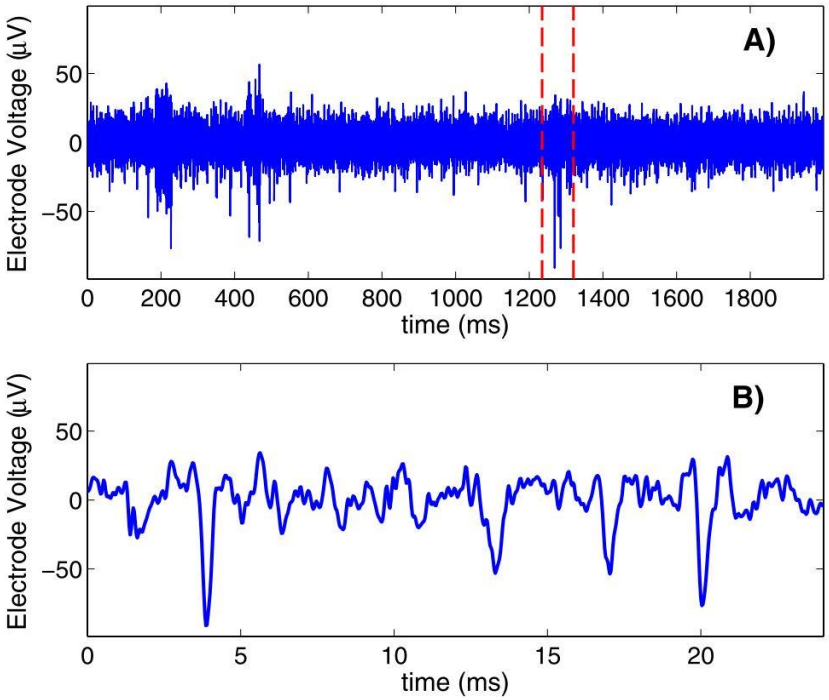

Figure 3.14. **A)** A 200ms recording of extracellular spiking activity recorded from a mouse olfactory bulb slice and a **B)** 25ms subset of **A**.

CONCLUSION

This paper has presented a highly scalable architecture and demonstration of a CMOS sensor array with metal electrodes and optical sensors. The design was based upon the characteristics of extracellularly recorded neural potentials. Due to a distributed ADC and a compact low-noise front-end amplifier, the system achieves a high-spatial resolution of 50μm without compromising recording area or sampling rate. The system requires simple postprocessing to encapsulate the wirebonds and platinize the aluminum electrodes for biocompatibility. The system can perform lensless imaging to localize external electrodes by computationally refocusing information from ASPs. Action potential and LFP recordings from a mouse olfactory bulb slice were also presented. The presented system will enable unique neurophysiological experiments on a chip.

ACKNOWLEDGMENT

The authors would like to thank MOSIS for fabrication support.

REFERENCES

1. Johnson, B., Peace, S. T., Cleland, T. A. & Molnar, A. A scalable CMOS sensor array for neuronal recording and imaging. in *2011 IEEE Sensors* 924–927 (IEEE, 2011). doi:10.1109/ICSENS.2011.6127268

2. Frey, U. *et al.* Switch-Matrix-Based High-Density Microelectrode Array in CMOS Technology. *IEEE J. Solid-State Circuits* **45,** 467–482 (2010).

3. Heer, F. *et al.* Single-chip microelectronic system to interface with living cells. *Biosens. Bioelectron.* **22,** 2546–2553 (2007).

4. Boyden, E. S., Zhang, F., Bamberg, E., Nagel, G. & Deisseroth, K. *Millisecond-timescale, genetically targeted optical control of neural activity*. 1263–1268 (Nature Publishing Group, 2005).

5. Wang, A., Gill, P. R. & Molnar, A. Fluorescent imaging and localization with angle sensitive pixel arrays in standard CMOS. in *2010 IEEE Sensors* 1706–1709 (2010). doi:10.1109/ICSENS.2010.5689914

6. Harrison, R. R. & Charles, C. A low-power low-noise CMOS amplifier for neural recording applications. *IEEE J. Solid-State Circuits* **38,** 958–965 (2003).

7. Gire, D. H. & Schoppa, N. E. Long-term enhancement of synchronized oscillations by adrenergic receptor activation in the olfactory bulb. *J. Neurophysiol.* **99,** 2021–2025 (2008).

8. Muller, R., Gambini, S. & Rabaey, J. M. A 0.013 , 5 , DC-Coupled Neural Signal Acquisition IC With 0.5 V Supply. *IEEE J. Solid-State Circuits* **47,** 232–243 (2012).

9. Zanos, T. P., Mineault, P. J. & Pack, C. C. Removal of Spurious Correlations Between Spikes and Local Field Potentials. *J. Neurophysiol.* **105,** 474–486 (2011).

10. David, S. V., Malaval, N. & Shamma, S. A. Decoupling action potential bias from cortical local field potentials. *Comput. Intell. Neurosci.* 393019 (2010). doi:10.1155/2010/393019

11. Yang, Z., Zhao, Q., Keefer, E. & Liu, W. Noise characterization, modeling, and reduction for in vivo neural recording. in *Advances in neural information processing systems* 2160–2168 (2009). at <http://papers.nips.cc/paper/3695-noise-characterization-modeling-and-reduction-for-in-vivo-neural-recording>

12. Joye, N., Schmid, A. & Leblebici, Y. A cell-electrode interface noise model for high-density microelectrode arrays. *Conf. Proc. Annu. Int. Conf. IEEE Eng. Med. Biol. Soc. IEEE Eng. Med. Biol. Soc. Annu. Conf.* **2009,** 3247–3250 (2009).

13. Franks, W., Schenker, I., Schmutz, P. & Hierlemann, A. Impedance characterization and modeling of electrodes for biomedical applications. *IEEE Trans. Biomed. Eng.* **52,** 1295–1302 (2005).

14. Frey, U. *et al.* Depth recording capabilities of planar high-density microelectrode arrays. in *4th International IEEE/EMBS Conference on Neural Engineering, 2009. NER '09* 207–210 (2009). doi:10.1109/NER.2009.5109270

15. Lindén, H. *et al.* Modeling the Spatial Reach of the LFP. *Neuron* **72,** 859–872 (2011).

16. Berdondini, L. *et al.* Active pixel sensor array for high spatio-temporal resolution electrophysiological recordings from single cell to large scale neuronal networks. *Lab. Chip* **9,** 2644–2651 (2009).

17. Lambacher, A. *et al.* Identifying firing mammalian neurons in networks with high-resolution multi-transistor array (MTA). *Appl. Phys. A* **102,** 1–11 (2010).

18. Aziz, J. N. *et al.* 256-channel neural recording and delta compression microsystem with 3D electrodes. *Solid-State Circuits IEEE J. Of* **44,** 995–1005 (2009).

19. Wang, A., Gill, P. R. & Molnar, A. An angle-sensitive CMOS imager for single-sensor 3D photography. in *Solid-State Circuits Conference Digest of Technical Papers (ISSCC), 2011 IEEE International* 412–414 (2011). doi:10.1109/ISSCC.2011.5746375

20. Wang, A. & Molnar, A. A Light-Field Image Sensor in 180 nm CMOS. *IEEE J. Solid-State Circuits* **47,** 257–271 (2012).

21. Dandin, M. *et al.* Post-CMOS packaging methods for integrated biosensors. in *2009 IEEE Sensors* 795–798 (2009). doi:10.1109/ICSENS.2009.5398540

22. Liu, Y., Smela, E., Nelson, N. M. & Abshire, P. Cell-lab on a chip: a CMOS-based microsystem for culturing and monitoring cells. *Conf. Proc. Annu. Int. Conf. IEEE Eng. Med. Biol. Soc. IEEE Eng. Med. Biol. Soc. Annu. Conf.* **4,** 2534–2537 (2004).

23. El-Rahman, S. S. A. Neuropathology of aluminum toxicity in rats (glutamate and GABA impairment). *Pharmacol. Res. Off. J. Ital. Pharmacol. Soc.* **47,** 189–194 (2003).

24. Steyaert, M. S. J. & Sansen, W. M. C. A micropower low-noise monolithic instrumentation amplifier for medical purposes. *IEEE J. Solid-State Circuits* **22,** 1163–1168 (1987)